Electrostatic gyrokinetic simulations in Wendelstein 7-X geometry: benchmark between the codes `stella` and `GENE`

A. González-Jerez[1]†, P. Xanthopoulos[2], J. M. García-Regaña[1], I. Calvo[1], J. Alcusón[2], A. Bañón Navarro[3], M. Barnes[4], F. I. Parra[4] and J. Geiger[2]

[1]Laboratorio Nacional de Fusión, CIEMAT, 28040, Madrid, Spain

[2]Max-Planck Institut für Plasmaphysik, 17491 Greifswald, Germany

[3]Max-Planck Institut für Plasmaphysik, 85748 Garching, Germany

[4]Rudolf Peierls Centre for Theoretical Physics, University of Oxford, Oxford OX1 3PU, UK

The first experimental campaigns have proven that, due to the optimization of the magnetic configuration with respect to neoclassical transport, the contribution of turbulence is essential to understand and predict the total particle and energy transport in Wendelstein 7-X (W7-X). This has spurred much work on gyrokinetic modelling for the interpretation of the available experimental results and for the preparation of the next campaigns. At the same time, new stellarator gyrokinetic codes have just been or are being developed. It is therefore desirable to have a sufficiently complete, documented and verified set of gyrokinetic simulations in W7-X geometry against which new codes or upgrades of existing codes can be tested and benchmarked. This paper attemps to provide such a set of simulations in the form of a comprehensive benchmark between the recently developed code `stella` and the well-established code `GENE`. The benchmark consists of electrostatic gyrokinetic simulations in W7-X magnetic geometry and includes different flux tubes, linear ion-temperature-gradient (ITG) and trapped-electron-mode (TEM) stability analyses, computation of linear zonal flow responses and calculation of ITG-driven heat fluxes.

1. Introduction

One of the main issues in magnetic confinement fusion plasmas is the theoretical understanding of turbulence and turbulent transport, attributable to the action of instabilities driven by density and temperature gradients. Since decades, turbulence is known to be the main source of transport in low collisionality tokamak plasmas. In stellarators, neoclassical transport at low collisionality is usually large, at least in the plasma core, and turbulence has sometimes been assumed to play a less important role. The first experimental campaigns of Wendelstein 7-X (W7-X) (Wolf *et al.* (2017); Klinger *et al.* (2019)) have made it evident that, in general, the total particle and energy transport is higher than predicted by neoclassical theory (Bozhenkov *et al.* 2020), turning turbulent transport into an essential mechanism to understand and predict these results. This disagreement between the experimental measurements and the predictions of neoclassical theory has motivated much work on gyrokinetic modelling, including upgrades of existing codes and development of new ones with the aim of understanding the first available experimental results of W7-X and preparing the next experimental campaigns.

† Email address for correspondence: AntonioG@ciemat.es

While existing tokamak gyrokinetic codes (Parker *et al.* (1993), Kotschenreuther *et al.* (1995), Lin (1998), Dorland *et al.* (2000), Jenko (2000), Candy & Waltz (2003), Jolliet *et al.* (2007), Peeters *et al.* (2009)) have been extensively exploited and tested, less work has been carried out in the validation and verification of stellarator gyrokinetic codes (Kornilov *et al.* (2004), Watanabe & Sugama (2005), Xanthopoulos & Jenko (2007), Baumgaertel *et al.* (2011), Cole *et al.* (2019), Barnes *et al.* (2019), Maurer *et al.* (2020), Wang *et al.* (2020)). In the context of verification between stellarator gyrokinetic codes, comparisons have also been reported. In Helander *et al.* (2015) the growth rate of linear ion-temperature-gradient-driven modes in W7-X computed with the global particle-in-cell code `EUTERPE` and with the full flux surface version of `GENE` are compared. These simulations have later been reproduced with the global particle-in-cell code `XGC-S` in Cole *et al.* (2019) and with the global version of `GENE`, `GENE-3D`, in Maurer *et al.* (2020). Although valuable, as they account for global effects, these efforts are limited to linear cases and a single type of instability. In this paper we provide a set of linear and nonlinear gyrokinetic simulations in W7-X geometry against which present and future stellarator gyrokinetic codes can be tested and benchmarked (following the example of the tokamak community with the Cyclone Base Case (Dimits *et al.* 2000)). It is presented in the form of a comprehensive benchmark between the recently developed flux-tube gyrokinetic code `stella` and the well-established code `GENE` in W7-X geometry. The most important difference between these two codes is the treatment of the parallel streaming and acceleration terms of the gyrokinetic Vlasov equation. The mixed implicit-explicit numerical scheme used by `stella` makes it possible to handle these terms implicitly, allowing a larger time step size in simulations with kinetic electrons. This turns `stella` into an efficient code for multispecies turbulence simulations in stellarators.

The rest of the paper is organized as follows. In section 2, the flux tube equations solved by `stella` and `GENE` are presented, as well as some relevant differences between their implementation in these two codes. In section 3, the W7-X magnetic configuration selected for our study is described together with the two flux tubes in which the simulations will be performed, the so-called *bean* and *triangular* flux tubes. The simulations of this paper are divided into five *tests* and the parameters used to carry out each one of them are also collected in this section. In section 4, the linear part of the study is performed, encompassing the first four tests. In tests 1 to 3, the values of growth rate and real frequency computed with `GENE` and `stella` are compared. Tests 1 and 2 assume adiabatic electrons, studying ITGs in the bean and triangular flux tubes, and test 3 includes kinetic electrons, studying density-gradient-driven TEMs in the bean flux tube. In these tests, the structure of the electrostatic potential is also given, discussing the features of each instability. The remarkable difference between the time step size required by `stella` and `GENE` in linear simulations with kinetic electrons is also emphasized. In test 4, the linear zonal flow response is computed with both codes, comparing four different time traces of the electrostatic potential relaxation. In section 5, nonlinear simulations results are given. They include the study of the ITG-driven heat flux and the contribution of each mode to this quantity, computed with `stella` in the bean and triangular flux tubes. The results obtained in the bean flux tube are compared with `GENE` calculations in test 5. Finally, section 6 contains the summary and the conclusions.

2. Equations solved by `stella` and `GENE`

The codes `stella` and `GENE` are based on the δf gyrokinetic theory, first proposed in Catto (1978). In the present paper, we use versions of these codes that solve the flux-tube gyrokinetic equations for stellarator electrostatic turbulence. The flux-tube

approach explicitly exploits the scale separation between the typical variation lengths of the background magnetic field and plasma profiles, and the typical spatial scales of the turbulent fluctuations in the plane perpendicular to the magnetic field. Next, we introduce the coordinates used along the paper and write the electrostatic flux-tube equations.

We consider stellarator configurations with nested magnetic surfaces and define spatial coordinates $\{r, \alpha, z\}$, where $r \in [0, a]$ is a radial coordinate that labels magnetic surfaces, $\alpha \in [0, 2\pi)$ is an angular coordinate labeling field lines on each magnetic surface and $z \in [z_{\min}, z_{\max}]$ is a coordinate along field lines. Here, a is the stellarator minor radius. The value $r = a$ corresponds to the *last closed flux surface*†. Specifically, we choose

$$r := a\sqrt{\frac{\psi_t}{\psi_{t,a}}}, \tag{2.1}$$

where $2\pi\psi_t(r)$ is the toroidal flux enclosed by the surface labeled by r and $\psi_{t,a} := \psi_t(a)$. As for α, we take

$$\alpha = \theta - \iota\zeta, \tag{2.2}$$

where θ and ζ are, respectively, the poloidal and toroidal PEST flux coordinates (Grimm *et al.* 1983) and $\iota(r)$ is the rotational transform. In these coordinates, the magnetic field can be expressed as

$$\mathbf{B} = \psi_t'\nabla r \times \nabla\alpha. \tag{2.3}$$

Throughout the paper, a prime ($'$) means differentiation with respect to r. Note that with our choice for r, we have

$$\psi_t'(r) = \frac{2\psi_{t,a}r}{a^2}. \tag{2.4}$$

It is also useful to define the quantity B_a, which will be used in this paper as a reference magnetic field and it is given by

$$\psi_{t,a} = \text{sgn}(\psi_{t,a})\frac{a^2 B_a}{2}, \tag{2.5}$$

where $\text{sgn}(\cdot)$ is the sign function, so that B_a is always positive.

Let r_0 and α_0 be the values of r and α that select a flux tube (and the center of the simulation domain). In the plane perpendicular to $\mathbf{B}$, stella and GENE use coordinates x and y defined as

$$x := r - r_0 \tag{2.6}$$

and

$$y := r_0(\alpha - \alpha_0), \tag{2.7}$$

whereas, along $\mathbf{B}$, stella takes $z = \zeta$ and GENE employs $z = \theta$. In velocity space, stella and GENE use $v_{||}$ and μ as independent coordinates, where $v_{||}$ is the component of the velocity parallel to the magnetic field line and $\mu = m_j v_\perp^2/2B$ is the magnetic moment, with $v_\perp$ the component of the velocity perpendicular to the magnetic field, $|\mathbf{B}| = B$ the magnetic field strength and m_j the mass, where the subscript j indicates the species. Here, j can take the values 'i', if it refers to ions, and 'e', if it refers to electrons. In coordinates $\{x, y, z, v_{||}, \mu\}$, the fluctuating distribution function of the species j can be

† Given the volume of the last closed flux surface, V_a, the minor radius can be defined as $a = \sqrt{V_a/2\pi^2 R_0}$, where $2\pi R_0$ is the length of the magnetic axis and R_0 is called the stellarator major radius. This definition of a coincides with the effective minor radius computed by VMEC (Hirshman 1983).

4 A. González-Jerez et al.

Fourier expanded as

$$g_j(x, y, z, v_\parallel, \mu, t) = \sum_{k_x, k_y} \hat{g}_{\mathbf{k}_\perp, j}(z, v_\parallel, \mu, t) e^{i(k_x x + k_y y)} \qquad (2.8)$$

and, equivalently, the fluctuating electrostatic potential can be expressed as

$$\varphi(x, y, z, t) = \sum_{k_x, k_y} \hat{\varphi}_{\mathbf{k}_\perp}(z, t) e^{i(k_x x + k_y y)}, \qquad (2.9)$$

where t is the time. The flux-tube gyrokinetic equation for the mode $\mathbf{k}_\perp$ of the fluctuating distribution function, $\hat{g}_{\mathbf{k}_\perp, j}$, reads

$$\partial_t \hat{g}_{\mathbf{k}_\perp, j} + v_\parallel \hat{\mathbf{b}} \cdot \nabla z \left(\partial_z \hat{g}_{\mathbf{k}_\perp, j} + \frac{Z_j e}{T_j} \partial_z \left[\varphi_{\mathbf{k}_\perp} J_0(k_\perp v_\perp / \Omega_j) \right] F_{0,j} \right) - \frac{\mu}{m_j} \hat{\mathbf{b}} \cdot \nabla B \partial_{v_\parallel} \hat{g}_{\mathbf{k}_\perp, j}$$

$$- i \frac{\mathrm{sgn}(\psi_{t,a}) k_y}{B_a} \left[\frac{n_j'}{n_j} + \frac{T_j'}{T_j} \left(\frac{m_j(v_\parallel^2/2 + B\mu/m_j)}{T_j} - \frac{3}{2} \right) \right] \hat{\varphi}_{\mathbf{k}_\perp} J_0(k_\perp v_\perp / \Omega_j) F_{0,j} \qquad (2.10)$$

$$+ \frac{i}{\Omega_j} \left(v_\parallel^2 \hat{\mathbf{b}} \times \boldsymbol{\kappa} + \frac{\mu}{m_j} \hat{\mathbf{b}} \times \nabla B \right) \cdot \mathbf{k}_\perp \left(\hat{g}_{\mathbf{k}_\perp, j} + \frac{Z_j e}{T_j} \hat{\varphi}_{\mathbf{k}_\perp} J_0(k_\perp v_\perp / \Omega_j) F_{0,j} \right) - N_{\mathbf{k}_\perp, j} = 0,$$

where B_a is given by (2.5), $n_j(r)$ and $T_j(r)$ are the density and temperature, assumed to be flux functions, $\Omega_j = Z_j e B / m_j$ is the gyrofrequency, Z_j is the charge number, e is the proton charge, $\mathbf{k}_\perp = k_x \nabla x + k_y \nabla y$ is the perpendicular wavevector,

$$F_{0,j} = n_j (m_j / 2\pi T_j)^{3/2} \exp\left[-m_j(v_\parallel^2/2 + \mu B/m_j)/T_j \right]$$

is a Maxwellian and J_0 is the zeroth order Bessel function of the first kind. Finally, $\boldsymbol{\kappa} = \hat{\mathbf{b}} \cdot \nabla \hat{\mathbf{b}}$ is the curvature vector, with $\hat{\mathbf{b}} = B^{-1} \mathbf{B}$ and $N_{\mathbf{k}_\perp, j}$ is the mode $\mathbf{k}_\perp$ of the nonlinear term, which can be written as

$$N_{\mathbf{k}_\perp, j} = \frac{\mathrm{sgn}(\psi_{t,a})}{B_a} \sum_{\substack{k_{x_1}, k_{y_1} \\ k_{x_2}, k_{y_2}}} (k_{x_1} k_{y_2} - k_{x_2} k_{y_1}) J_0(k_{\perp_1} v_\perp / \Omega_j) \hat{\varphi}_{\mathbf{k}_{\perp_1}} \hat{g}_{\mathbf{k}_{\perp_2}, j},$$

where $\mathbf{k}_{\perp_1} = k_{x_1} \nabla x + k_{y_1} \nabla y$ and $\mathbf{k}_{\perp_2} = k_{x_2} \nabla x + k_{y_2} \nabla y$ are such that $\mathbf{k}_{\perp_1} + \mathbf{k}_{\perp_2} = \mathbf{k}_\perp$. The quasineutrality equation reads

$$\sum_j \frac{Z_j B}{m_j} \int_{-\infty}^{\infty} \mathrm{d}v_\parallel \int_0^{\infty} \mathrm{d}\mu J_0(k_\perp v_\perp / \Omega_j) \hat{g}_{\mathbf{k}_\perp, j}$$

$$+ \sum_j \frac{Z_j^2 e n_j}{2\pi T_j} \left(\Gamma_0 \left(\frac{k_\perp^2 v_{th,j}^2}{2\Omega_j^2} \right) - 1 \right) \hat{\varphi}_{\mathbf{k}_\perp} = 0, \qquad (2.11)$$

where $v_{th,j} = \sqrt{2T_j/m_j}$ is the thermal speed and $\Gamma_0(b) = \exp(-b) I_0(b)$ with I_0 the zeroth order modified Bessel function of the first kind. In (2.10) and (2.11), geometric quantities, as well as the plasma profiles and their derivatives, are evaluated at r_0 and α_0. Both stella and GENE read the geometric quantities required to solve the gyrokinetic equations from a VMEC output.

Despite solving the same equations (2.10) and (2.11), there are some differences between stella and GENE when implementing them. We will only mention the most relevant ones and refer the reader to Barnes et al. (2019) and Merz (2009) for further details. The main difference is the treatment of the parallel streaming and acceleration terms in equation (2.10). For electrons, these terms of the gyrokinetic Vlasov equation

a [m]	R_0 [m]	r_0/a	B_a [T]	$\iota(r_0)$	$-\frac{r_0}{\iota(r_0)}\frac{d\iota}{dr}(r_0)$
0.494	5.485	0.8	2.604	0.910	-0.107

Table 1: Basic quantities of the magnetic configuration and the flux surface selected for the simulations. From left to right: minor radius, major radius, selected flux surface, reference magnetic field given by (2.5), rotational transform and global magnetic shear.

scale up to a factor $\sqrt{m_i/m_e}$ with respect to the other terms. This imposes severe restrictions on the time step size in explicit methods when performing simulations with kinetic electrons. GENE treats these terms explicitly, while stella computes them implicitly, allowing to handle kinetic electrons using a time step size only slightly smaller than the one employed in simulations with adiabatic electrons, greatly reducing the computational cost. This will be clearly shown in section 4, where simulations with kinetic electrons are presented. Finally, different boundary conditions have been used by each code in linear simulations. Whereas stella employs a zero incoming boundary condition on the fluctuating distribution function, $\hat{g}_{\mathbf{k}_\perp,j}(z_{\min}, v_\parallel > 0) = \hat{g}_{\mathbf{k}_\perp,j}(z_{\max}, v_\parallel < 0) = 0$, GENE uses *twist and shift* boundary conditions (Beer *et al.* 1995).

3. Configuration and parameters

The flexible set of planar and non-planar coils of W7-X allows a large variety of magnetic configurations. Depending on the values that some quantities take (by appropriately choosing the currents in the coil system), different names are used for each configuration. For instance, the value of ι allows to distinguish between *high-* and *low-iota* configurations, in which ι at the boundary is 5/4 and 5/6, respectively, and the magnetic configuration naturally develops the corresponding island structures. Similarly, depending on the toroidal mirror ratio† we have *high-* and *low-mirror* configurations. The *standard* configuration (in which all planar coil currents are set to zero and the non-planar coil currents are set to the same value) and the high-mirror configuration feature particularly reduced levels of neoclassical transport and bootstrap current, respectively. These facts, in part, explain why they are the configurations most commonly employed for experiments and simulations (for a detailed description of the physical and technical features of W7-X configurations see Geiger *et al.* (2015)). In this work, we will use a high-mirror configuration. For future electromagnetic extensions of this benchmark and because W7-X aims at operating at high $\langle\beta\rangle$ (Klinger *et al.* 2019), we have considered a high-mirror equilibrium with $\langle\beta\rangle \approx 3\%$. Specifically, the equilibrium is based on a fixed-boundary VMEC-calculation. This means that it does not use the coils definition file mgrid but employs a simplified high-mirror vacuum configuration boundary. Some basic quantities of this magnetic configuration and the flux surface selected for our simulations are listed in table 1. In Appendix A, the input parameters necessary to produce this fixed-boundary equilibrium with VMEC are provided.

In stellarators, different magnetic field lines on a flux surface are not equivalent. In general, gyrokinetic simulations run on different flux tubes lead to different results. For this reason, this work includes simulations in two different flux tubes, the one that extends

† The toroidal mirror ratio is defined as $b_{01} \equiv B_{01}/B_{00}$ in a Fourier representation B_{mn} of the magnetic field strength, where m and n are, respectively, poloidal and toroidal mode numbers. In different configurations of W7-X this ratio can range, approximately, from 0 to 0.1.
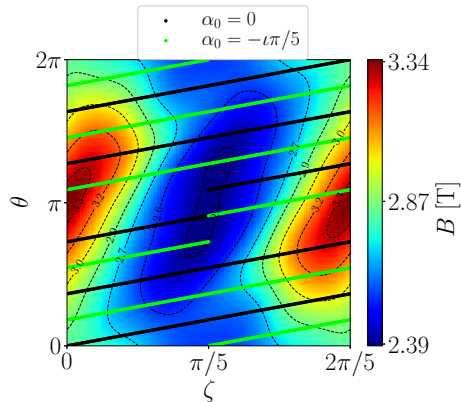
Figure 1: Schematic view of the magnetic field lines $\alpha_0 = 0$ (solid black line) and $\alpha_0 = -\iota\pi/5$ (solid green line) extended along the five field periods of W7-X. The magnetic field strength is represented in the background.
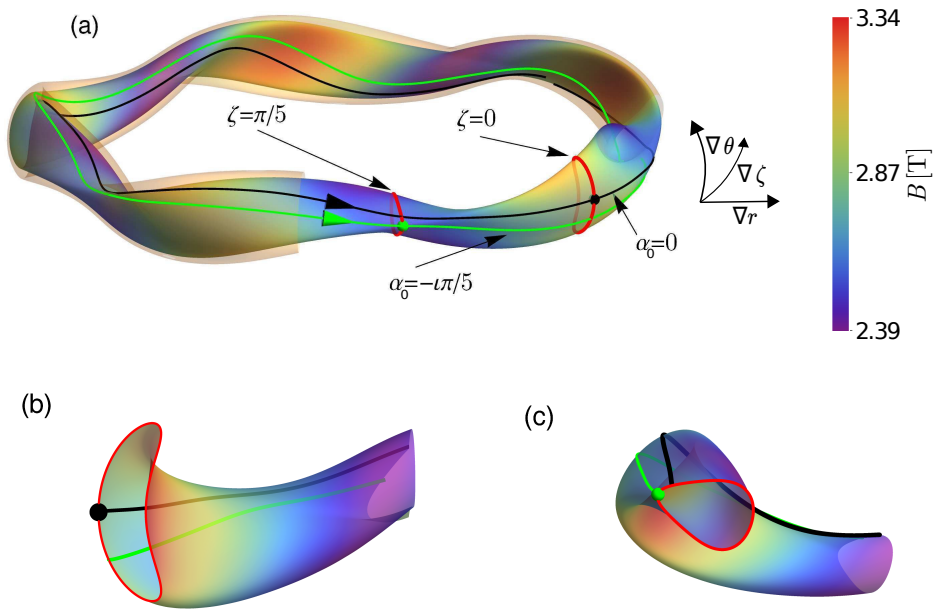

Figure 2: 3D view of the surface $r_0/a = 0.8$ (a), together with the field line $\alpha_0 = 0$ (solid black line), the field line $\alpha_0 = -\iota\pi/5$ (solid green line) and the last closed flux surface $r_0 = a$ as a semi-transparent halo. Details of two toroidal cuts of the flux surface $r_0/a = 0.8$ are also given, showing a bean-shaped section (b) and a triangular section (c).
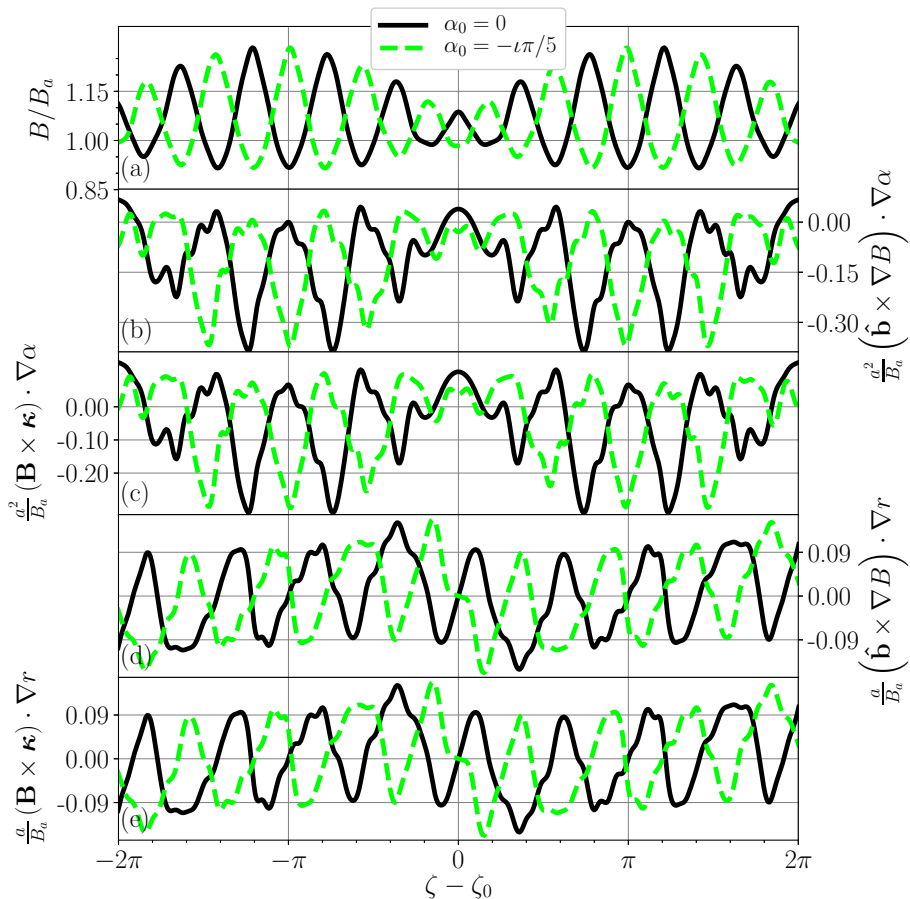
Figure 3: Normalized geometric quantities in the range $\zeta - \zeta_0 = [-2\pi, 2\pi]$ for the surface $r_0/a = 0.8$ along the field lines $\alpha_0 = 0$ (solid black line) and $\alpha_0 = -\iota\pi/5$ (dashed green line). The magnetic field strength is represented in (a); the projections of $\hat{\mathbf{b}} \times \nabla B$ and $\mathbf{B} \times \boldsymbol{\kappa}$ along the binormal direction are represented in (b) and (c), respectively; the projections of $\hat{\mathbf{b}} \times \nabla B$ and $\mathbf{B} \times \boldsymbol{\kappa}$ along the radial direction are represented in (d) and (e), respectively.

along the widely simulated field line $\alpha_0 = 0$ and the less common choice $\alpha_0 = -\iota\pi/5$. The field line $\alpha_0 = 0$ is centered with respect to the so-called equatorial plane, $\theta = 0$, and the bean-shaped toroidal plane $\zeta = 0$, hence the name bean flux tube. The field line $\alpha_0 = -\iota\pi/5$ is centered with respect to the equatorial plane and the triangular toroidal plane $\zeta = \pi/5$, hence the name triangular flux tube. A schematic view of these field lines for the flux surface $r_0/a = 0.8$ is given in figure 1, where they are represented on a (θ, ζ) plane with the magnetic field strength referred to the color scale. A 3D view of the surface $r_0/a = 0.8$ is shown in figure 2 (a) together with a sketch of our choice of flux coordinates and the field lines $\alpha_0 = 0$ and $\alpha_0 = -\iota\pi/5$. Figures 2 (b) and 2 (c) show some details of figure 2 (a). The geometric quantities required to solve equations (2.10) and (2.11) for the mentioned flux tubes are represented against the ζ coordinate, centered with respect to $\zeta_0 = \zeta(\theta = 0)$, in figures 3 (a)-(e). In figure 3 (a) it is observed that the magnetic

	Flux tube	$\left[N_\theta^m, N_\theta^M\right]$	a/L_{T_i}	a/L_{n_i}	$N_{v_\parallel}$	N_μ	$N_{\mathbf{k}_\perp, j}$	$\Delta t v_{th,i}/a$	Compared
Test 1.	bean	[1 , 6]	3	1	36	24	Off	stella 0.15 GENE 0.14	$\gamma(k_x)$, $\omega(k_x)$ $\gamma(k_y)$, $\omega(k_y)$
Test 2.	triangular	[4 , 6]	3	1	36	24	Off	stella 0.15 GENE 0.14	$\gamma(k_x)$, $\omega(k_x)$
Test 3.	bean	[2 , 8]	0	3	36	24	Off	stella 0.04 GENE 0.004	$\gamma(k_y)$, $\omega(k_y)$ $|\hat\varphi_{\mathbf{k}_\perp}|(z)$
Test 4.	bean	[4 , 4]	0	0	256	32	Off	stella 0.15 GENE 0.1	$\langle \mathrm{Re}(\hat\varphi_{\mathbf{k}_\perp})\rangle_z(t)$
Test 5.	bean††	[1 , 1]	3	1	60	24	On	stella 0.09 GENE 0.09	$Q_i(t)$ $\sum_{k_y} Q_i(k_x, k_y)$ $\sum_{k_x} Q_i(k_x, k_y)$

Table 2: Set of parameters used in each test. From left to right: flux tube, minimum and maximum number of N_θ, normalized ion temperature and density gradients, number of divisions in the grid of $v_\parallel$ and μ, presence of nonlinear term, time step size and quantities compared with both codes.

field strength is symmetric with respect to $\zeta = \zeta_0$. This symmetry is also seen in the quantities $\left(\hat{\mathbf{b}} \times \nabla B\right) \cdot \nabla \alpha$ and $(\mathbf{B} \times \boldsymbol{\kappa}) \cdot \nabla \alpha$, which are represented in figures 3 (b) and 3 (c), respectively. In figures 3 (d) and 3 (e) we see that $(\mathbf{B} \times \boldsymbol{\kappa}) \cdot \nabla r = \left(\hat{\mathbf{b}} \times \nabla B\right) \cdot \nabla r$, as is the case for any ideal MHD equilibria. In what follows, we will refer to the direction of $\nabla \alpha$ as binormal direction and to the direction of ∇r as radial direction. The description of the flux tubes is complete with the specification of their length, which has been defined as the number of turns in the poloidal direction, N_θ. This length is chosen to correctly resolve the electrostatic potential $\hat\varphi_{\mathbf{k}_\perp}$ along the flux tube. Since the localization of the electrostatic potential varies with the wavenumber, different values of N_θ have been considered in each test. The maximum and minimum values of N_θ, N_θ^M and N_θ^m, respectively, needed in each test are indicated in table 2, together with other parameters that define the simulations. These include the normalized ion temperature and density gradients†

$$a/L_{T_i} := -a \left(\ln T_i\right)' \qquad (3.1)$$

and

$$a/L_{n_i} := -a \left(\ln n_i\right)', \qquad (3.2)$$

the number of divisions in the velocity grid $(N_{v_\parallel}, N_\mu)$, the presence of nonlinear term $(N_{\mathbf{k}_\perp, j})$, the time step size used for the calculation of the most unstable mode in each simulation and the different quantities compared in each test, where γ refers to the growth rate, ω refers to the real frequency, $\langle \cdot \rangle_z$ means a line average and Q_i is the ion heat flux. It is important to remark that we have always considered $128 \times N_\theta$ divisions in the grid of z. In addition, $Z_i = 1$ and $T_i/T_e = 1$ have been assumed. In what follows, the results of

† The normalized electron temperature and density gradients are set to zero, $a/L_{T_e} = a/L_{n_e} = 0$, for every test with adiabatic electrons, which excludes test 3. The values given to these quantities in test 3 will be specified in section 4.

†† Nonlinear results obtained with stella in the triangular flux tube are also included in section 5.
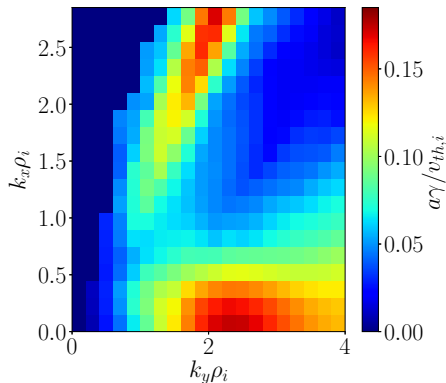
Figure 4: ITG stability map corresponding to test 1. It shows the growth rate computed with the code `stella` in the bean flux tube as a function of k_x and k_y.

the tests are expressed in the coordinates $\{x, y, z\}$ used by `stella`, i.e., the ones defined in expressions (2.6) and (2.7) with $z = \zeta$.

4. Linear simulations

To perform a linear flux-tube gyrokinetic simulation, both codes solve the system of equations consisting of (2.10) and (2.11) dropping the nonlinear term of (2.10) and assuming $\hat{g}_{\mathbf{k}_\perp}$ and $\hat{\varphi}_{\mathbf{k}_\perp}$ to be proportional to $\exp\left[(\gamma - \mathrm{i}\omega)t\right]$, where γ and ω are the growth rate and real frequency of each mode. In this section, four different linear tests are presented. In tests 1 and 2, ion-temperature-gradient-driven modes (ITGs) are simulated. In test 3, density-gradient-driven trapped-electron-modes (TEMs) are computed. Finally, the simulations of test 4 include the collisionless relaxation of a zonal electrostatic potential.

The linear properties of ITGs and TEMs in stellarators have been reported in a large number of studies by means of linear gyrokinetic simulations. Kornilov *et al.* (2004) studied the ITG structure and its stability in W7-X with the global particle-in-cell code `EUTERPE`. This code has also been used to model the effects of radial electric fields on ITG modes for the geometries of W7-X and the Large Helical Device (LHD) in Riemann *et al.* (2016). Xanthopoulos & Jenko (2007) and Proll *et al.* (2013) used the code `GENE` to study the effect of changes in the density gradient and temperature ratio on ITGs and TEMs and to look at the stability properties of W7-X, comparing with other devices. `GENE` has also been used in Proll *et al.* (2015) to investigate how stellarators can be optimized with respect to TEMs and in Alcusón *et al.* (2020) to analyze the growth rate of the instability as a function of the temperature and density scales for different configurations of W7-X. A theoretical study about the effects of ITGs and TEMs in non-axisymmetric devices and, particularly in W7-X is summarized in Helander *et al.* (2015). Recently, in Sánchez *et al.* (2021), the codes `EUTERPE`, `GENE`, `stella` and `GENE-3D` have been compared in order to assess the differences on the linear properties of ITGs and the zonal flow relaxation that arise when different computational domain, namely, flux tube, full flux surface and radially global domain, are considered.
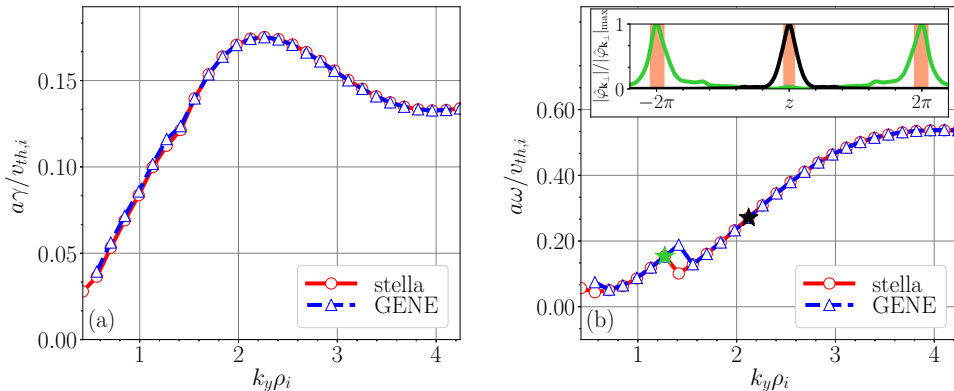
Figure 5: Linear growth rate (a) and real frequency (b) as a function of k_y obtained for the ITG scenario studied in test 1 using `stella` (open circles linked by a solid red line) and `GENE` (open triangles linked by a dashed blue line) in the bean flux tube. The inset of figure (b) shows the structure of the modes $(k_x\rho_i, k_y\rho_i) = (0, 1.3)$ (green line) and $(k_x\rho_i, k_y\rho_i) = (0, 2.1)$ (black line) together with some bad curvature regions (shaded in red).

4.1. *Test 1. Linear ITG simulations in the bean flux tube*

In this test, a linear ITG driven by a normalized ion temperature gradient $a/L_{T_i} = 3$ with a normalized ion density gradient $a/L_{n_i} = 1$ and adiabatic electrons is simulated in the bean flux tube (see table 2). In order to find the most unstable mode, a map containing the growth rate values as a function of the radial and binormal wavenumbers has been produced with `stella` and shown in figure 4. Note that the ion thermal Larmor gyroradius, ρ_i, is used for the normalization of wavevector components and it is defined as

$$\rho_i = \frac{v_{th,i}m_i}{Z_i e B_a}. \tag{4.1}$$

Two regions of large growth rate can be observed in this map. While $N_\theta = 1$ is enough to simulate the region with $k_x\rho_i \lesssim 0.5$, $N_\theta = 6$† is required to simulate the one including $k_x\rho_i \gtrsim 2$ due to the displacement in the z direction of the parallel structure of the modes. The maximum growth rate found in this map is localized at $k_y\rho_i = 2.1$. The codes `GENE` and `stella` have been used to compare the spectrum along k_y for fixed k_x and vice-versa, capturing this wavenumber in both scans.

The comparison of growth rates and real frequencies as a function of k_y for fixed $k_x = 0$ is given in figures 5 (a) and 5 (b), respectively. These figures show an excellent agreement between `stella` and `GENE`. In figure 5 (b) it is seen that the frequency is positive for every simulated mode. ITG-driven modes are expected to propagate in the ion diamagnetic direction, i.e. $\omega\omega_{*,i} > 0$, where $\omega_{*,i}$ is the ion diamagnetic frequency, which, with our definitions and conventions, reads

$$\omega_{*,i} = -\text{sgn}(\psi_{t,a})\frac{T_i k_y}{Z_i e B_a L_{n_i}}. \tag{4.2}$$

As only positive values of k_y are explored in this scan, $L_{n_i} > 0$ (see table 2) and $\psi_{t,a} < 0$ for the selected configuration (see the direction of **B** and the left-handed system sketched

† These lengths are the required ones if the flux tube is centered at $z = 0$.
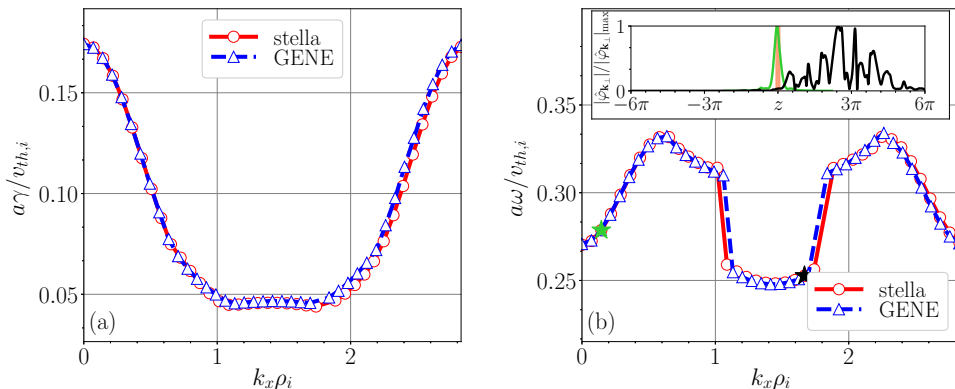
Figure 6: Linear growth rate (a) and real frequency (b) as a function of k_x obtained for the ITG scenario studied in test 1 using `stella` (open circles linked by a solid red line) and `GENE` (open triangles linked by a dashed blue line) in the bean flux tube. The inset of figure (b) shows the structure of the modes $(k_x\rho_i, k_y\rho_i) = (0.2, 2.1)$ (green line) and $(k_x\rho_i, k_y\rho_i) = (1.7, 2.1)$ (black line), together with a bad curvature region (shaded in red).

in figure 2 (a)), we have $\omega_{*,i} > 0$. This proves that, indeed, in this test $\omega\omega_{*,i} > 0$, thus the studied ITG-driven modes propagate in the ion diamagnetic direction. A closer look at figure 5 (b) shows a discontinuity in the frequency, which is associated with a change in the mode structure, defining two different branches of the ITG instability. This can be observed in the inset of figure 5 (b), which represents, as a function of z, computations of `stella` for the the modulus of the electrostatic potential normalized to its maximum value $(|\hat{\varphi}_{\mathbf{k}_\perp}|/|\hat{\varphi}_{\mathbf{k}_\perp}|_{\max})$ for the modes with $k_y\rho_i = \{1.3, 2.1\}$. These modes are strongly localized in the highlighted red bands, which correspond to *bad curvature* regions, defined as those where

$$\frac{k_y T_i'}{\psi_t'}\left(\hat{\mathbf{b}} \times \nabla B\right) \cdot \mathbf{k}_\perp > 0. \tag{4.3}$$

If $k_x = 0$ and $k_y > 0$ these regions are the ones where the quantity shown in figure 3 (b) takes positive values. The growth rates and real frequencies as a function of k_x, keeping $k_y\rho_i = 2.1$, can be seen in figures 6 (a) and 6 (b), respectively. As in the k_y-spectra, every mode studied in this scan propagates in the ion diamagnetic direction, as it can be observed in figure 6 (b). This figure also shows a discontinuity in the frequency, giving rise to three different branches, located at $k_x\rho_i \in (0, 1.0]$, $k_x\rho_i \in (1.0, 1.8)$ and $k_x\rho_i \in [1.8, 2.7)$. In the inset of figure 6 (b), the structure of the modes with $k_x\rho_i = \{0.2, 1.7\}$ computed with `stella`, belonging to the first and central branches, respectively, are represented as a function of z. As observed in this inset, the electrostatic potential associated to the first branch is strongly localized and $N_\theta = 1$ has been sufficient to capture the parallel structure of this mode. On the other hand, the electrostatic potential associated to the central branch spreads along z, making it necessary to extend the flux tube length up to $N_\theta = 6$.
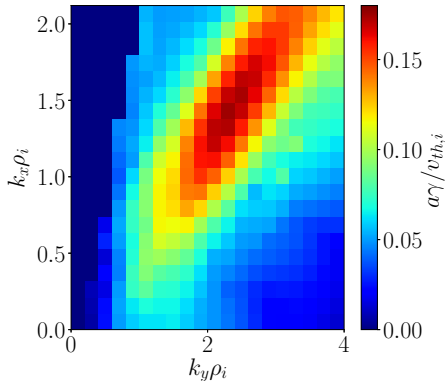
Figure 7: ITG stability map corresponding to test 2. It shows the growth rate computed with the code `stella` in the triangular flux tube as a function of k_x and k_y.

4.2. *Test 2. Linear ITG simulations in the triangular flux tube*

In this test, a linear ITG instability driven by a normalized ion temperature gradient $a/L_{T_i} = 3$ with a normalized ion density gradient $a/L_{n_i} = 1$ and adiabatic electrons is simulated in the triangular flux tube (see table 2) .

As in the previous test, in order to find the most unstable mode, a map of the growth rate for each pair (k_x, k_y) has been produced with `stella`, see figure 7. As in the bean flux tube, the most unstable mode in this map is localized at $k_y \rho_i = 2.1$. Interestingly, unlike in the bean flux tube, the maximum growth rate does not correspond to a mode with $k_x = 0$. This figure also shows the triangular flux tube to be equally unstable as the bean one as $\gamma_{\text{bean}}^{\max}/\gamma_{\text{triang}}^{\max} \simeq 1$. The different localization in k_x of the most unstable modes found in figures 4 and 7 implies that special care must be taken when comparing the linear stability properties of different flux tubes.

A scan along k_x, keeping $k_y \rho_i = 2.1$, has been performed with both codes, representing the growth rates and real frequencies in figures 8 (a) and 8 (b), respectively. Although not as close as in the bean flux tube, the agreement between `stella` and `GENE` is still remarkable. As in the previous test, these modes propagate in the ion diamagnetic direction. In this scan, the localization of the electrostatic potential moves to higher values of z when increasing k_x, making it necessary to extend the flux tube length up to $N_\theta = 6$. The inset of figure 8 (b) includes the parallel structure of the mode with $k_x \rho_i = 1.2$ obtained with `stella`, together with the bad curvature region where this mode is localized.

4.3. *Test 3. Linear density-gradient-driven TEM simulations in the bean flux tube*

In the third test, kinetic electrons are included. We study linear instabilities driven by normalized electron and ion density gradients $a/L_{n_e} = a/L_{n_i} = 3$. In order to avoid the presence of temperature gradient driven modes, the electron and ion temperature gradients have been set to zero, $a/L_{T_e} = a/L_{T_i} = 0$ (see table 2). We will refer to modes studied in this subsection as density-gradient-driven TEMs. It is worth noting (see $\Delta t v_{\text{th},i}/a$ in table 2) how the mixed implicit-explicit method employed by `stella` allows a larger time step in these simulations than the explicit scheme used in `GENE`. This difference in the time step size results in a clear reduction of the total simulated time. In fact, while `GENE` has required 703 total CPU hours (5.49 hours running in 128
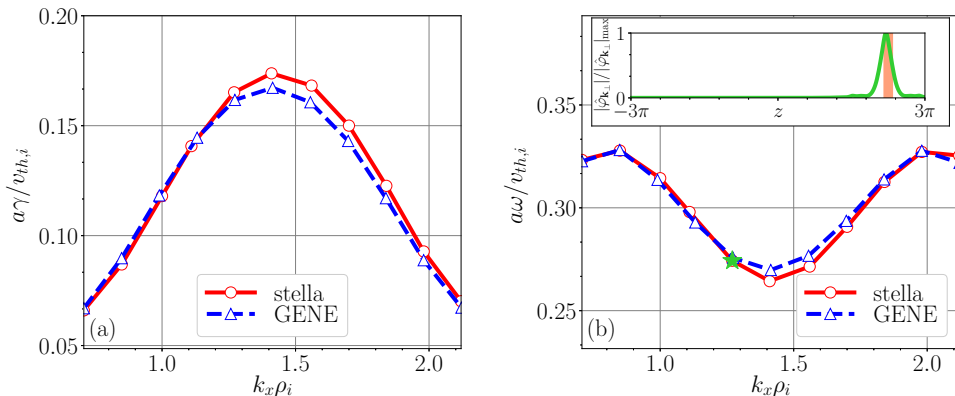
Figure 8: Linear growth rate (a) and real frequency (b) as a function of k_x obtained for the ITG scenario studied in test 2 using `stella` (open circles linked by a solid red line) and `GENE` (open triangles linked by a dashed blue line) in the triangular flux tube. The inset of figure (b) shows the structure of the mode $(k_x\rho_i, k_y\rho_i) = (1.2, 2.1)$ (green line) together with a bad curvature region (shaded in red).

processors) to complete the whole simulation, `stella` has needed 76 total CPU hours (0.53 hours running in 144 processors) to simulate the same modes. The growth rate and real frequency values as a function of k_y, keeping $k_x = 0$, are shown in figures 9 (a) and 9 (b), respectively. As observed in these figures, there is a remarkable agreement between the results obtained with `stella` and `GENE`. In figure 9 (b) it can be seen that these modes can propagate both in the electron† and ion diamagnetic directions, depending on the wavenumber. A closer look at this figure allows to clearly distinguish three different branches. The electrostatic potentials associated to the modes with $k_y\rho_i = \{0.7, 1.2, 4.7\}$, belonging each one to a different branch, are represented as a function of z for the whole length of the flux tube in figures 10 (a), (c) and (e), obtaining a good agreement between both codes. The same structures found in figures 10 (a), (c) and (e) are represented in figures 10 (b), (d) and (f), respectively, in a narrower z range, together with the normalized magnetic field strength and the bad curvature regions. The parallel structure of the modes belonging to the first branch, in the range $k_y\rho_i = (0, 1.1]$, has a particular shape (figures 10 (a) and 10 (b)), which can be identified with some structures discussed in Proll (2014). To resolve this electrostatic potential we have increased the flux tube length up to $N_\theta = 8$ with both codes. In order to study the second branch, in the narrow range of $k_y\rho_i = (1.0, 1.5)$, the flux tube has been extended up to $N_\theta = 4$. Finally, $N_\theta = 2$ has been sufficient for the study of the third branch, covering from $k_y\rho_i = 1.4$ to the end of the simulated range.

4.4. Test 4. Zonal-flow relaxation in the bean flux tube

Finally, we address the so-called Rosenbluth-Hinton test (Rosenbluth & Hinton 1998), which consists in the study of the linear collisionless time evolution of the zonal components of the potential, i.e. those with $k_y = 0$, from their value at the initial time $t = 0$ to their value when $t \to \infty$. The theoretical study of the zonal flow response in stellarators has been addressed in Sugama & Watanabe (2005); Mishchenko *et al.* (2008); Helander *et al.* (2011); Monreal *et al.* (2016); Monreal *et al.* (2017) and Smoniewski *et al.*

---

† Since $Z_i = 1$ and $T_i/T_e = 1$, we have $\omega_{*,e} = -\omega_{*,i}$.
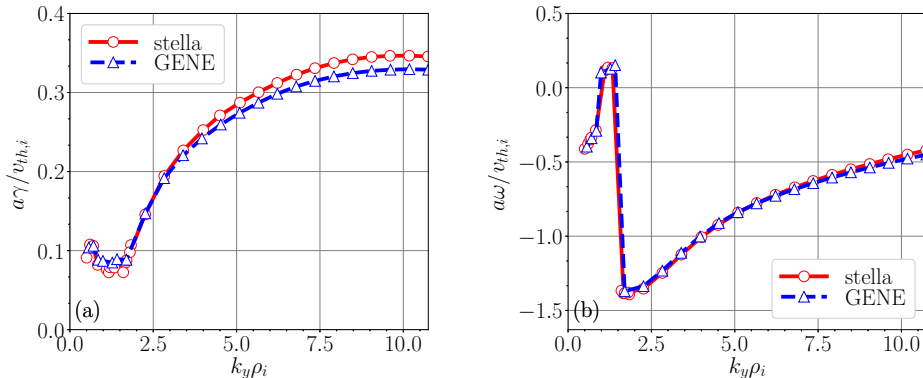
Figure 9: Linear growth rate (a) and real frequency (b) as a function of k_y obtained for the instabilities studied in test 3 using `stella` (open circles linked by a solid red line) and `GENE` (open triangles linked by a dashed blue line) in the bean flux tube.

(2021). In non-axisymmetric devices, the relaxation of a zonal potential perturbation typically shows a damped oscillation, reaching a stationary residual level at $t \to \infty$. The damped oscillation involves two different frequencies with different time scales: the geodesic acoustic mode (GAM) oscillation (which is also found in tokamaks) and a low frequency oscillation characteristic of the non-axisymmetric geometry of the stellarator. This characteristic low frequency oscillation of the time evolution of the potential, only predicted for $k_x \rho_i \ll 1$ (Mishchenko *et al.* (2008); Helander *et al.* (2011); Monreal *et al.* (2017)), has been experimentally identified in the TJ-II stellarator in Alonso *et al.* (2017).

For simplicity, in the simulations included in this test $a/L_{T_i} = a/L_{n_i} = 0$ have been considered. In addition, as initial condition we have imposed $\hat{\varphi}_{\mathbf{k}_\perp}(t = 0)$ to be a Gaussian function centered in the middle of the flux tube. Four time traces of the line averaged electrostatic potential normalized to its value at $t = 0$ have been computed and represented in figures 11 (a)-(d). In these figures, it can be observed how the results obtained with both codes for $k_x \rho_i \in \{0.05, 0.07, 0.1, 0.3\}$ match remarkably well. As already mentioned, the four time traces show an initial GAM oscillation at $t v_{th,i}/a < 100$, followed, except for figure 11 (d), by a lower-frequency damped oscillation. As observed in these figures, the frequency of the damped oscillation decreases with increasing k_x, in fact, for $k_x \rho_i = 0.3$, represented in figure 11 (d), this frequency is missing. The residual level of each time trace is given in the insets of these figures. These plots show that the residual value of the time traces increases with k_x.

5. Nonlinear simulations

In flux tube nonlinear simulations, the codes solve equations (2.10) and (2.11) within a flux tube that extends in the radial and binormal directions. The parameters that define the flux tube for the nonlinear test presented in this section (test 5) are listed in table 3. First nonlinear gyrokinetic simulations in W7-X were reported by Xanthopoulos *et al.* (2007), where `GENE` was used to study the nonlinear ITG-driven heat flux. Since then, `GENE` has been widely used to look at the nonlinear properties of turbulence in W7-X (Xanthopoulos *et al.* (2011); Helander *et al.* (2015)). More recently, in Bañón-Navarro *et al.* (2020), the effects of ITG turbulent transport in different configurations of W7-X have been investigated with the global version of `GENE`, `GENE-3D` (Maurer *et al.* 2020).
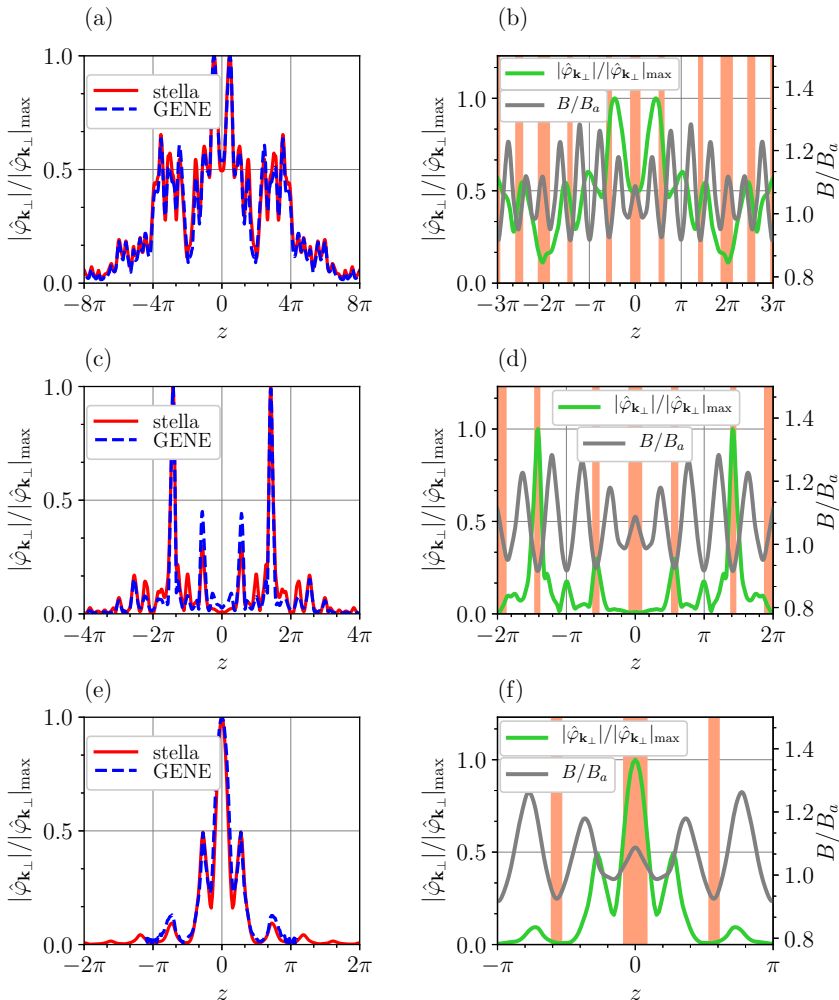
Figure 10: Normalized modulus of the electrostatic potential computed with `stella` (solid red line) and `GENE` (dashed blue line) as a function of z over the entire length of the flux tube for some modes simulated in test 3; specifically, we are representing the modes $(k_x \rho_i, k_y \rho_i) = (0, 0.7)$ (a), $(0, 1.2)$ (c) and $(0, 4.7)$ (e). The structures calculated with `stella` are shown as solid green lines in narrower z ranges in figures (b), (d) and (f), respectively, together with the normalized magnetic field strength (grey line) and the bad curvature regions (shaded in red).

In (Sánchez *et al.* 2020) the ITG-driven heat flux has been studied using realistic plasma parameters with the global particle-in-cell gyrokinectic code `EUTERPE`. Finally, simulations carried out with `stella` with all species treated kinetically have been employed to look at the transport of impurities driven by ITG and TEM turbulence in W7-X (García-Regaña *et al.* 2021).
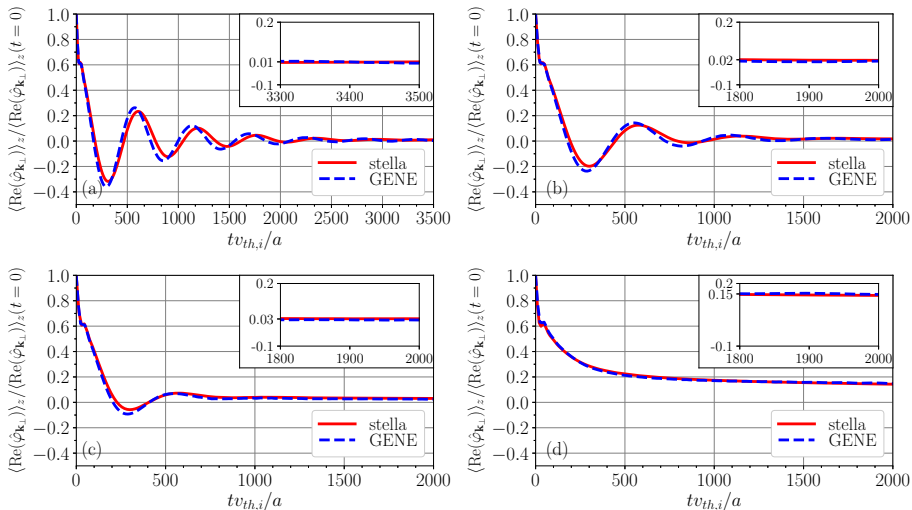
Figure 11: For test 4, time trace of the line-averaged electrostatic potential normalized to its maximum value computed with `stella` (solid red line) and with `GENE` (dashed blue line) for the pairs $(k_x\rho_i, k_y\rho_i) = (0.05, 0)$ (a), $(k_x\rho_i, k_y\rho_i) = (0.07, 0)$ (b), $(k_x\rho_i, k_y\rho_i) = (0.1, 0)$ (c) and $(k_x\rho_i, k_y\rho_i) = (0.3, 0)$ (d). The insets show a detail of each trace at large times.

Test 5.	l_x/ρ_i	l_y/ρ_i	N_{k_x}	N_{k_y}	$|k_x|_{\min}\rho_i$	$k_{y,\min}\rho_i$
`stella`	99.9	62.8	51	64	0.067	0.100
`GENE`	131.3	88.6	101	64	0.047	0.071

Table 3: Parameters used by `stella` and `GENE` to define the flux tube in test 5. From left to right: normalized flux tube size in the radial (l_x) and binormal (l_y) directions; number of modes in the radial (N_{k_x}) and binormal (N_{k_y}) directions; smallest positive wavenumber in the radial ($|k_x|_{\min}$) and binormal ($k_{y,\min}$) directions.

5.1. *Test 5. Nonlinear ITG-driven heat flux*

In this test, a nonlinear calculation of the ITG-driven heat flux is carried out considering adiabatic electrons. In addition, a normalized ion temperature gradient $a/L_{T_i} = 3$ and a normalized ion density gradient $a/L_{n_i} = 1$ are assumed (see tables 2 and 3 for the values of the simulation parameters). The heat fluxes presented in this test are defined by

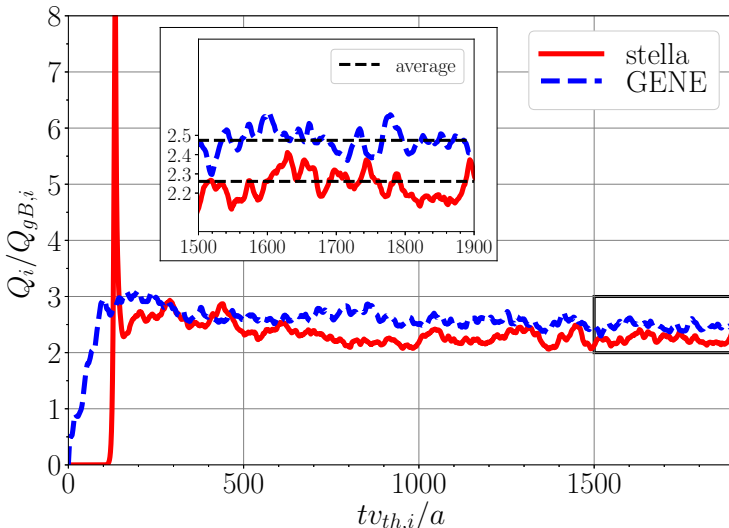$$Q_i = \left\langle \int d^3v \frac{m_i v^2}{2} \mathbf{v}_E \cdot \nabla r g_i \right\rangle, \tag{5.1}$$

Figure 12: Time trace of the normalized ITG-driven heat flux computed with `stella` (solid red line) and `GENE` (dashed blue line) in the bean flux tube for the test 5 ITG scenario. The inset shows a detail of the time interval $tv_{th,i}/a = [1500, 1900]$, with the heat flux time average given by the black dashed lines.

where $\langle \cdot \rangle$ is the flux-surface average, g_i is given by (2.8) and $\mathbf{v}_E$ is the turbulent $E \times B$ drift. In a flux tube, expression (5.1) takes the form

$$Q_i = \frac{\pi \operatorname{sgn}(\psi_{t,a})}{B_a} \left(\int_{z_{\min}}^{z_{\max}} \frac{\mathrm{d}z}{\mathbf{B} \cdot \nabla z} \right)^{-1} \int_{z_{\min}}^{z_{\max}} \mathrm{d}z \int_{-\infty}^{\infty} \mathrm{d}v_{\parallel} \int_{0}^{\infty} \mathrm{d}\mu \left[\left(v_{\parallel}^2 + \frac{2B\mu}{m_i} \right) \right.$$

$$\left. \sum_{k_x, k_y} \left(\operatorname{Im} \left(\hat{\varphi}_{\mathbf{k}_{\perp}} \hat{g}_{-\mathbf{k}_{\perp}, i} \right) k_y J_0(k_{\perp} v_{\perp}/\Omega_i) \right) \left(\hat{\mathbf{b}} \cdot \nabla z \right)^{-1} \right]. \tag{5.2}$$

The time trace of the ITG-driven heat flux computed with both codes and normalized to the ion gyro-Bohm heat flux, $Q_{gB,i} = n_i T_i v_{th,i} (\rho_i/a)^2$, is shown in figure 12. Despite the different initial evolution, both traces converge to very similar values. To quantify the difference between the saturated ITG-driven heat flux obtained with each code, an average over the time interval $tv_{th,i}/a = [1500, 1900]$ has been taken and represented in the inset of figure 12. The results for the normalized time-averaged ITG-driven heat flux computed with `stella`, which is $Q_i/Q_{gB,i} = 2.26$ and `GENE`, which is $Q_i/Q_{gB,i} = 2.47$, represent a difference around 8.5%. This slight difference may be caused by the different resolution in the flux tube used by each code, see table 3.

In order to provide a more comprehensive study of these results, `stella` has been used to compute the contribution of each pair (k_x, k_y) to the time-averaged ITG-driven heat flux. In figure 13, it can be observed that the modes which contribute the most to the heat flux are those with $k_y \rho_i \lesssim 2.0$ and $|k_x \rho_i| \lesssim 0.5$. To compare these results with `GENE` calculations, the time-averaged ITG-driven heat flux is represented as a function of k_y, summing over k_x, in figure 14 (a), and as function of k_x, summing over k_y, in figure 14 (b). These figures show a satisfactory agreement between both codes.

Finally, for the sake of completeness, a simulation in the triangular flux tube performed
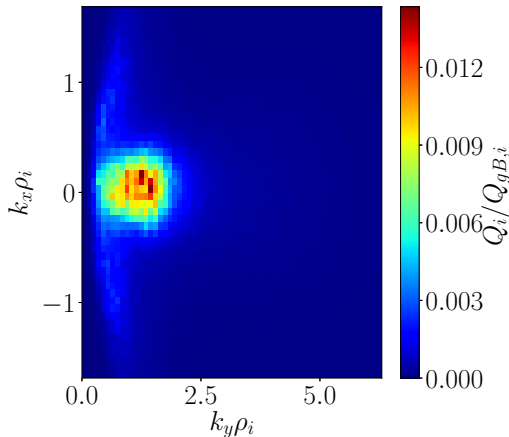
Figure 13: Normalized nonlinear ITG-driven heat flux computed with `stella` in the bean flux tube, averaged over the time interval $tv_{th,i}/a = [1500, 1900]$ and represented as a function of k_x and k_y.
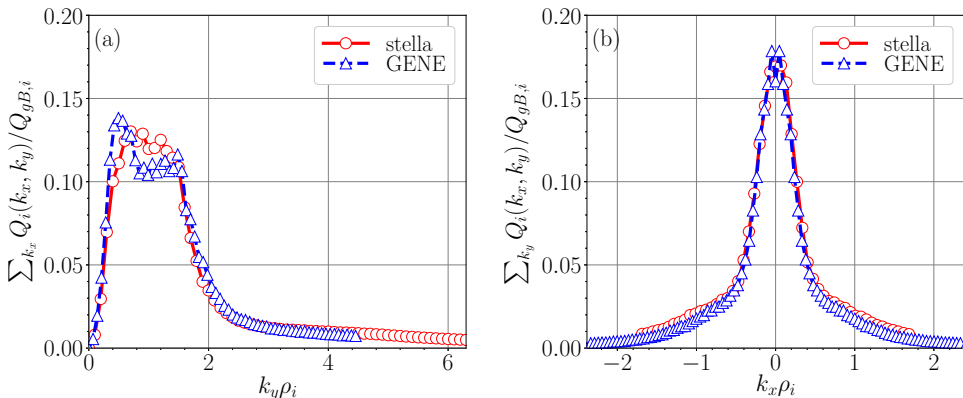

Figure 14: Normalized ITG-driven heat flux averaged over the time interval $tv_{th,i}/a = [1500, 1900]$ computed with `stella` (open circles linked by a solid red line) and `GENE` (open triangles linked by a dashed blue line) in the bean flux tube. It is represented as a function of k_y, summing over k_x (a) and as a function of k_x, summing over k_y (b).

with `stella` has been included in this section. The parameters selected to carry this simulation out are the ones collected in tables 2 and 3 for test 5. The time trace of the normalized ITG-driven heat flux and the contribution of each mode are represented in figures 15 (a) and 15 (b), respectively. Figure 15 (a) shows the saturated ITG-driven heat flux in the triangular flux tube to be $Q_i/Q_{gB,i} = 2.22$. This value is very similar to the one obtained in the bean flux tube using `stella`. The main differences between nonlinear ITG-driven heat flux calculations in both flux tubes are found in their spectrum, as it can be seen by comparing the maps given in figures 13 and 15 (b). As in the bean flux tube, the modes in the binormal direction which contribute the most to the total heat flux in the triangular flux tube are those with $k_y\rho_i \lesssim 2.0$. However, in contrast with the results
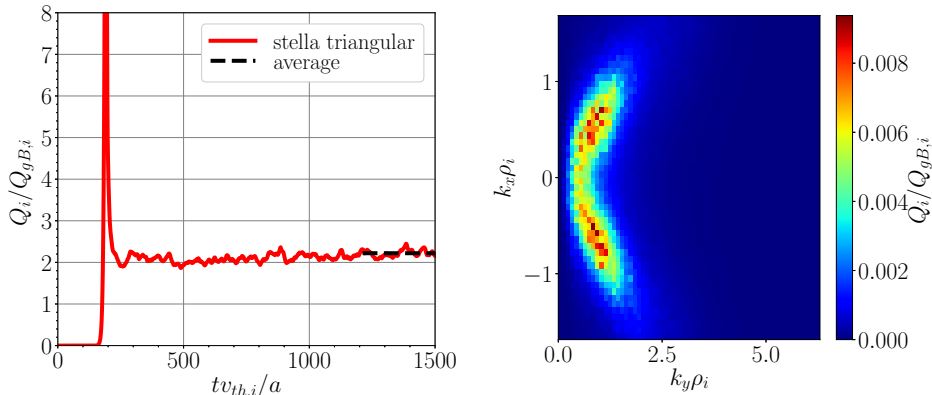
Figure 15: Time trace of the normalized ITG-driven heat flux computed with `stella` in the triangular flux tube, together with the heat flux time average over $tv_{th,i}/a = [1200, 1500]$, represented with a black dashed line (a). This time-averaged ITG-driven heat flux is also represented as a function of k_x and k_y (b).

Flux tube	$t_{\text{wall}-\text{clock}}$ [h]	N_{proc}	t_{CPU} [h]
Bean	`stella` 161 `GENE` 24	`stella` 288 `GENE` 1920	`stella` 46368 `GENE` 46080
Triangular	`stella` 115	`stella` 288	`stella` 33120

Table 4: Time required to run the nonlinear simulations with `GENE` in the bean flux tube and with `stella` in the bean and triangular flux tubes. From left to right: simulation wall-clock time in hours, number of processors and total CPU time in hours.

obtained for the bean flux tube, modes in the radial direction with $0.5 \lesssim |k_x \rho_i| \lesssim 1.5$ give a large contribution to the total heat flux in the triangular flux tube.

For a complete view of these nonlinear simulations, we have indicated in table 4 the simulation wall-clock time ($t_{\text{wall}-\text{clock}}$) required to produce these results. This table also includes the number of processors (N_{proc}) in which the codes have been running and the total CPU time (t_{CPU}) that each simulation has taken, defined as $t_{\text{CPU}} = N_{\text{proc}} \times t_{\text{wall}-\text{clock}}$. As expected, since we have assumed adiabatic electrons in these nonlinear calculations, both codes require similar t_{CPU} to perform the presented nonlinear test, as it is shown in table 4. On the other hand, the time difference when simulating the triangular and bean flux tubes with `stella` is attributable to the different time ranges explored with each simulation, see figures 12 and 15 (left).

6. Summary and conclusions

Due to the increasing interest in stellarator gyrokinetic modelling, fostered by the results of W7-X first experimental campaigns, it is desirable to have a sufficiently complete, documented and well verified set of linear and nonlinear gyrokinetic simulations in W7-X geometry against which present and future stellarator gyrokinetic codes can be tested and benchmarked. In this paper, such a set of simulations has been provided

in the form of a comprehensive benchmark between the codes `stella` and `GENE`. This benchmark, consisting of five different tests, has been carried out in a fixed-boundary high-mirror configuration of W7-X. The linear part of the benchmark has been presented in tests 1 to 4. ITG instabilities have been studied in the bean and triangular flux tubes of W7-X in tests 1 and 2, respectively. Comparing these results, it can be concluded that both flux tubes are equally unstable, but the largest growth rates are found at different radial wavenumbers. TEM instabilities driven by density gradients have been studied in test 3, where it has been shown how the mixed implicit-explicit method used by `stella` allows to use larger time steps than explicit codes for simulations with kinetic electrons, resulting in a clear reduction of the total CPU time. In these three tests, the structure of the electrostatic potential associated with each instability has been given and the growth rate and real frequency values obtained with `stella` and `GENE` have been successfully compared. In test 4, different time traces of the zonal electrostatic potential relaxation have been compared. Finally, the nonlinear ITG-driven heat flux and its spectrum have been calculated in test 5 in the bean flux tube with both codes and, for completeness, in the triangular flux tube with `stella`. The computed energy fluxes are similar in both flux tubes, although the radial modes that give the largest contribution to the total heat flux are different.

Acknowledgments

Declaration of interest

The authors report no conflict of interest.

Appendix A. VMEC parameters to reproduce the studied equilibria

In this appendix, the list of input parameters used to generate the fixed-boundary VMEC equilibrium used in the present work is provided (see the beginning of section 3):

```
&INDATA
 MGRID_FILE = ''
 LFREEB     = F
 LWOUTTXT   = T
 LDIAGNO    = T
 DELT       = 0.9
 TCON0      = 2.
 NFP        = 5
 NCURR      = 1
 MPOL       = 12        NTOR =   12
```

```
NZETA       = 36
NS_ARRAY    = 9  28   99
NITER       = 3700
NSTEP       = 100
NVACSKIP    = 6
GAMMA       = 0.
FTOL_ARRAY  = 0.  1.E-10  1.E-14
PHIEDGE     = 2.0
BLOAT       = 1.
CURTOR      = 0.
SPRES_PED   = 1.
AM          = 179370 -179370
AI          = 0.36 -0.062 0.0712 -0.025 0. 0. 0. 0. 0. 0. 0.
AC          = 0. 0. 0. 0. 0. 0. 0. 0. 0. 0.
RAXIS       = 5.5395 0.37547 0.01698 0.0014216 0.000027606
ZAXIS       = 0. -0.31289 -0.019191 -0.00044262 0.000034742
 RBC( 0,  0)= 5.5021E+00   ZBS( 0,  0)= 0.0000E+00
 RBC( 1,  0)= 2.8455E-01   ZBS( 1,  0)=-2.4009E-01
 RBC( 2,  0)=-5.7247E-03   ZBS( 2,  0)= 1.9753E-03
 RBC( 3,  0)=-3.4624E-04   ZBS( 3,  0)= 2.2597E-03
 RBC( 4,  0)=-1.4722E-03   ZBS( 4,  0)= 1.7290E-03
 RBC(-4,  1)=-7.8450E-04   ZBS(-4,  1)=-7.6096E-06
 RBC(-3,  1)=-1.4587E-04   ZBS(-3,  1)= 1.2663E-03
 RBC(-2,  1)= 1.5679E-03   ZBS(-2,  1)= 6.9395E-03
 RBC(-1,  1)= 1.8726E-02   ZBS(-1,  1)= 1.6401E-02
 RBC( 0,  1)= 4.8197E-01   ZBS( 0,  1)= 6.0460E-01
 RBC( 1,  1)=-2.1345E-01   ZBS( 1,  1)= 1.9431E-01
 RBC( 2,  1)=-2.1789E-02   ZBS( 2,  1)= 1.8594E-02
 RBC( 3,  1)= 1.4488E-03   ZBS( 3,  1)=-1.1209E-03
 RBC( 4,  1)= 1.4451E-03   ZBS( 4,  1)=-7.5419E-04
 RBC(-4,  2)= 1.4744E-04   ZBS(-4,  2)= 1.5260E-04
 RBC(-3,  2)= 2.9997E-04   ZBS(-3,  2)=-2.6406E-05
 RBC(-2,  2)= 2.0710E-03   ZBS(-2,  2)=-2.4917E-05
 RBC(-1,  2)= 1.0333E-02   ZBS(-1,  2)= 7.7931E-03
 RBC( 0,  2)= 3.5672E-02   ZBS( 0,  2)=-2.0312E-03
 RBC( 1,  2)= 4.3441E-02   ZBS( 1,  2)= 1.9773E-02
 RBC( 2,  2)= 6.6787E-02   ZBS( 2,  2)=-4.9779E-02
 RBC( 3,  2)=-2.1551E-04   ZBS( 3,  2)= 1.6853E-03
 RBC( 4,  2)=-5.9507E-04   ZBS( 4,  2)= 7.7889E-04
 RBC(-4,  3)= 1.5743E-04   ZBS(-4,  3)=-2.1339E-04
 RBC(-3,  3)=-1.4708E-04   ZBS(-3,  3)= 3.1735E-06
 RBC(-2,  3)=-1.2572E-04   ZBS(-2,  3)= 6.1239E-04
 RBC(-1,  3)= 1.5997E-03   ZBS(-1,  3)=-2.9522E-04
 RBC( 0,  3)=-2.0732E-03   ZBS( 0,  3)=-1.8327E-03
 RBC( 1,  3)=-1.1519E-02   ZBS( 1,  3)=-4.6829E-03
 RBC( 2,  3)=-2.0190E-02   ZBS( 2,  3)= 6.7910E-03
 RBC( 3,  3)=-1.3317E-02   ZBS( 3,  3)= 1.1217E-02
 RBC( 4,  3)= 1.2037E-03   ZBS( 4,  3)=-8.0214E-04
 RBC(-4,  4)=-3.6955E-06   ZBS(-4,  4)= 1.2264E-04
 RBC(-3,  4)= 1.9747E-04   ZBS(-3,  4)=-1.7509E-04
 RBC(-2,  4)= 9.2916E-05   ZBS(-2,  4)= 6.5936E-05
 RBC(-1,  4)=-4.2286E-04   ZBS(-1,  4)= 2.4530E-05
 RBC( 0,  4)= 1.9963E-03   ZBS( 0,  4)= 4.5823E-04
 RBC( 1,  4)=-1.2553E-03   ZBS( 1,  4)= 1.7370E-03
 RBC( 2,  4)= 8.1636E-03   ZBS( 2,  4)= 8.8024E-03
 RBC( 3,  4)= 3.0460E-03   ZBS( 3,  4)=-4.6653E-03
 RBC( 4,  4)= 5.0489E-04   ZBS( 4,  4)=-1.5253E-03
```

REFERENCES

ALCUSÓN, J.A., XANTHOPOULOS, P., PLUNK, G.G., HELANDER, P., WILMS, F., TURKIN, Y., VON STECHOW, A. & GRULKE, O. 2020 Suppression of electrostatic micro-instabilities in maximum-J stellarators. *Plasma Physics and Controlled Fusion* **62** (3), 035005.

ALONSO, J.A., SÁNCHEZ, E., CALVO, I., VELASCO, J.L., MCCARTHY, K.J., CHMYGA, A., ELISEEV, L.G., ESTRADA, T., KLEIBER, R., KRUPNIK, L.I., MELNIKOV, A.V., MONREAL, P., PARRA, F.I., PERFILOV, S. & ZHEZHERA, A.I. 2017 Observation of oscillatory radial electric field relaxation in a helical plasma. *Physical Review Letters* **118** (18).

BAÑÓN-NAVARRO, A., MERLO, G., PLUNK, G.G., XANTHOPOULOS, P., VON STECHOW, A., SIENA, A. DI, MAURER, M., HINDENLANG, F., WILMS, F. & JENKO, F. 2020 Global gyrokinetic simulations of ITG turbulence in the magnetic configuration space of the Wendelstein 7-X stellarator. *Plasma Physics and Controlled Fusion* **62** (10), 105005.

BARNES, M., PARRA, F.I. & LANDREMAN, M. 2019 stella: An operator-split, implicit–explicit δf-gyrokinetic code for general magnetic field configurations. *Journal of Computational Physics* **391**, 365–380.

BAUMGAERTEL, J.A., BELLI, E.A., DORLAND, W., GUTTENFELDER, W., HAMMETT, G.W., MIKKELSEN, D.R., REWOLDT, G., TANG, W. M. & XANTHOPOULOS, P. 2011 Simulating gyrokinetic microinstabilities in stellarator geometry with GS2. *Physics of Plasmas* **18** (12), 122301.

BEER, M.A., COWLEY, S.C. & HAMMETT, G.W. 1995 Field-aligned coordinates for nonlinear simulations of tokamak turbulence. *Physics of Plasmas* **2** (7), 2687–2700.

BOZHENKOV, S.A., KAZAKOV, Y., FORD, O.P., BEURSKENS, M.N.A., ALCUSÓN, J., ALONSO, J.A., BALDZUHN, J., BRANDT, C., BRUNNER, K.J., DAMM, H., FUCHERT, G., GEIGER, J., GRULKE, O., HIRSCH, M., HÖFEL, U., HUANG, Z., KNAUER, J., KRYCHOWIAK, M., LANGENBERG, A., LAQUA, H.P., LAZERSON, S., MARUSHCHENKO, N. B., MOSEEV, D., OTTE, M., PABLANT, N., PASCH, E., PAVONE, A., PROLL, J.H.E., RAHBARNIA, K., SCOTT, E.R., SMITH, H.M., STANGE, T., VON STECHOW, A., THOMSEN, H., TURKIN, YU., WURDEN, G., XANTHOPOULOS, P., ZHANG, D. & AND, R.C. WOLF 2020 High-performance plasmas after pellet injections in Wendelstein 7-X. *Nuclear Fusion* **60** (6), 066011.

CANDY, J. & WALTZ, R.E. 2003 An eulerian gyrokinetic-Maxwell solver. *Journal of Computational Physics* **186** (2), 545–581.

CATTO, P.J. 1978 Linearized gyro-kinetics. *Plasma Physics* **20** (7), 719–722.

COLE, M.D.J., HAGER, R., MORITAKA, T., DOMINSKI, J., KLEIBER, R., KU, S., LAZERSON, S.A., RIEMANN, J. & CHANG, C.S. 2019 Verification of the global gyrokinetic stellarator code XGC-S for linear ion temperature gradient driven modes. *Physics of Plasmas* **26** (8), 082501.

DIMITS, A.M., BATEMAN, G., BEER, M.A., COHEN, B.I., DORLAND, W., HAMMETT, G.W., KIM, C., KINSEY, J.E., KOTSCHENREUTHER, M., KRITZ, A.H., LAO, L.L., MANDREKAS, J., NEVINS, W.M., PARKER, S.E., REDD, A.J., SHUMAKER, D.E., SYDORA, R. & WEILAND, J. 2000 Comparisons and physics basis of tokamak transport models and turbulence simulations. *Physics of Plasmas* **7** (3), 969–983.

DORLAND, W., JENKO, F., KOTSCHENREUTHER, M. & ROGERS, B.N. 2000 Electron temperature gradient turbulence. *Physical Review Letters* **85** (26), 5579–5582.

GARCÍA-REGAÑA, J.M., BARNES, M., CALVO, I., PARRA, F.I., ALCUSÓN, J.A., DAVIES, R., GONZÁLEZ-JEREZ, A., MOLLÉN, A., SÁNCHEZ, E., VELASCO, J.L. & ZOCCO, A. 2021 Turbulent impurity transport simulations in Wendelstein 7-X plasmas. *Journal of Plasma Physics* **87** (1), 85587010.

GEIGER, J., BEIDLER, C.D., FENG, Y., MAASSBERG, H., MARUSHCHENKO, N.B. & TURKIN, Y. 2015 Physics in the magnetic configuration space of W7-X. *Plasma Physics and Controlled Fusion* **57** (1), 014004.

GRIMM, R.C., DEWAR, R.L. & MANICKAM, J. 1983 Ideal MHD stability calculations in axisymmetric toroidal coordinate systems. *Journal of Computational Physics* **49** (1), 94–117.

HELANDER, P., BIRD, T., JENKO, F., KLEIBER, R., PLUNK, G.G., PROLL, J.H.E., RIEMANN,

J. & Xanthopoulos, P. 2015 Advances in stellarator gyrokinetics. *Nuclear Fusion* **55** (5), 053030.

Helander, P, Mishchenko, A, Kleiber, R & Xanthopoulos, P 2011 Oscillations of zonal flows in stellarators. *Plasma Physics and Controlled Fusion* **53** (5), 054006.

Hirshman, S.P. 1983 Steepest-descent moment method for three-dimensional magnetohydrodynamic equilibria. *Physics of Fluids* **26** (12), 3553.

Jenko, Frank 2000 Massively parallel vlasov simulation of electromagnetic drift-wave turbulence. *Computer Physics Communications* **125** (1-3), 196–209.

Jolliet, S., Bottino, A., Angelino, P., Hatzky, R., Tran, T.M., Mcmillan, B.F., Sauter, O., Appert, K., Idomura, Y. & Villard, L. 2007 A global collisionless PIC code in magnetic coordinates. *Computer Physics Communications* **177** (5), 409–425.

Klinger, T., Andreeva, T., Bozhenkov, S., Brandt, C., Burhenn, R., Buttenschön, B., Fuchert, G., Geiger, B., Grulke, O., Laqua, H.P., Pablant, N., Rahbarnia, K., Stange, T., von Stechow, A., Tamura, N., Thomsen, H., Turkin, Y., Wegner, T., Abramovic, I., Äkäslompolo, S., Alcuson, J., Aleynikov, P., Aleynikova, K., Ali, A., Alonso, A., Anda, G., Ascasibar, E., Bähner, J.P., Baek, S.G., Balden, M., Baldzuhn, J., Banduch, M., Barbui, T., Behr, W., Beidler, C., Benndorf, A., Biedermann, C., Biel, W., Blackwell, B., Blanco, E., Blatzheim, M., Ballinger, S., Bluhm, T., Böckenhoff, D., Böswirth, B., Böttger, L.-G., Borchardt, M., Borsuk, V., Boscary, J., Bosch, H.-S., Beurskens, M., Brakel, R., Brand, H., Bräuer, T., Braune, H., Brezinsek, S., Brunner, K.-J., Bussiahn, R., Bykov, V., Cai, J., Calvo, I., Cannas, B., Cappa, A., Carls, A., Carralero, D., Carraro, L., Carvalho, B., Castejon, F., Charl, A., Chaudhary, N., Chauvin, D., Chernyshev, F., Cianciosa, M., Citarella, R., Claps, G., Coenen, J., Cole, M., Cole, M.J., Cordella, F., Cseh, G., Czarnecka, A., Czerski, K., Czerwinski, M., Czymek, G., da Molin, A., da Silva, A., Damm, H., de la Pena, A., Degenkolbe, S., Dhard, C.P., Dibon, M., Dinklage, A., Dittmar, T., Drevlak, M., Drewelow, P., Drews, P., Durodie, F., Edlund, E., van Eeten, P., Effenberg, F., Ehrke, G., Elgeti, S., Endler, M., Ennis, D., Esteban, H., Estrada, T., Fellinger, J., Feng, Y., Flom, E., Fernandes, H., Fietz, W.H., Figacz, W., Fontdecaba, J., Ford, O., Fornal, T., Frerichs, H., Freund, A., Funaba, T., Galkowski, A., Gantenbein, G., Gao, Y., Regaña, J. García, Gates, D., Geiger, J., Giannella, V., Gogoleva, A., Goncalves, B., Goriaev, A., Gradic, D., Grahl, M., Green, J., Greuner, H., Grosman, A., Grote, H., Gruca, M., Guerard, C., Hacker, P., Han, X., Harris, J.H., Hartmann, D., Hathiramani, D., Hein, B., Heinemann, B., Helander, P., Henneberg, S., Henkel, M., Sanchez, J. Hernandez, Hidalgo, C., Hirsch, M., Hollfeld, K.P., Höfel, U., Hölting, A., Höschen, D., Houry, M., Howard, J., Huang, X., Huang, Z., Hubeny, M., Huber, M., Hunger, H., Ida, K., Ilkei, T., Illy, S., Israeli, B., Jablonski, S., Jakubowski, M., Jelonnek, J., Jenzsch, H., Jesche, T., Jia, M., Junghanns, P., Kacmarczyk, J., Kallmeyer, J.-P., Kamionka, U., Kasahara, H., Kasparek, W., Kazakov, Y.O., Kenmochi, N., Killer, C., Kirschner, A., Kleiber, R., Knauer, J., Knaup, M., Knieps, A., Kobarg, T., Kocsis, G., Köchl, F., Kolesnichenko, Y., Könies, A., König, R., Kornejew, P., Koschinsky, J.-P., Köster, F., Krämer, M., Krampitz, R., Krämer-Flecken, A., Krawczyk, N., Kremeyer, T., Krom, J., Krychowiak, M., Ksiazek, I., Kubkowska, M., Kühner, G., Kurki-Suonio, T., Kurz, P.A., Kwak, S., Landreman, M., Lang, P., Lang, R., Langenberg, A., Langish, S., Laqua, H., Laube, R., Lazerson, S., Lechte, C., Lennartz, M., Leonhardt, W., Li, C., Li, C., Li, Y., Liang, Y., Linsmeier, C., Liu, S., Lobsien, J.-F., Loesser, D., Cisquella, J. Loizu, Lore, J., Lorenz, A., Losert, M., Lücke, A., Lumsdaine, A., Lutsenko, V., Maassberg, H., Marchuk, O., Matthew, J.H., Marsen, S., Marushchenko, M., Masuzaki, S., Maurer, D., Mayer, M., McCarthy, K., McNeely, P., Meier, A., Mellein, D., Mendelevitch, B., Mertens, P., Mikkelsen, D., Mishchenko, A., Missal, B., Mittelstaedt, J., Mizuuchi, T., Mollen, A., Moncada, V., Mönnich, T., Morisaki, T., Moseev, D., Murakami, S., Náfrádi, G., Nagel, M., Naujoks, D., Neilson, H., Neu, R., Neubauer, O., Neuner, U., Ngo, T., Nicolai, D., Nielsen, S.K., Niemann, H., Nishizawa, T., Nocentini, R., Nührenberg, C., Nührenberg, J., Obermayer, S., Offermanns,

G., Ogawa, K., Ölmanns, J., Ongena, J., Oosterbeek, J.W., Orozco, G., Otte, M., Rodriguez, L. Pacios, Panadero, N., Alvarez, N. Panadero, Papenfuss, D., Paqay, S., Pasch, E., Pavone, A., Pawelec, E., Pedersen, T.S., Pelka, G., Perseo, V., Peterson, B., Pilopp, D., Pingel, S., Pisano, F., Plaum, B., Plunk, G., Pölöskei, P., Porkolab, M., Proll, J., Puiatti, M.-E., Sitjes, A. Puig, Purps, F., Rack, M., Récsei, S., Reiman, A., Reimold, F., Reiter, D., Remppel, F., Renard, S., Riedl, R., Riemann, J., Risse, K., Rohde, V., Röhlinger, H., Romé, M., Rondeshagen, D., Rong, P., Roth, B., Rudischhauser, L., Rummel, K., Rummel, T., Runov, A., Rust, N., Ryc, L., Ryosuke, S., Sakamoto, R., Salewski, M., Samartsev, A., Sanchez, E., Sano, F., Satake, S., Schacht, J., Satheeswaran, G., Schauer, F., Scherer, T., Schilling, J., Schlaich, A., Schlisio, G., Schluck, F., Schlüter, K.-H., Schmitt, J., Schmitz, H., Schmitz, O., Schmuck, S., Schneider, M., Schneider, W., Scholz, P., Schrittwieser, R., Schröder, M., Schröder, T., Schroeder, R., Schumacher, H., Schweer, B., Scott, E., Sereda, S., Shanahan, B., Sibilia, M., Sinha, P., Siplä, S., Slaby, C., Sleczka, M., Smith, H., Spiess, W., Spong, D.A., Spring, A., Stadler, R., Stejner, M., Stephey, L., Stridde, U., Suzuki, C., Svensson, J., Szabó, V., Szabolics, T., Szepesi, T., Szökefalvi-Nagy, Z., Tancetti, A., Terry, J., Thomas, J., Thumm, M., Travere, J.M., Traverso, P., Tretter, J., Mora, H. Trimino, Tsuchiya, H., Tsujimura, T., Tulipán, S., Unterberg, B., Vakulchyk, I., Valet, S., Vano, L., van Milligen, B., van Vuuren, A.J., Vela, L., Velasco, J.-L., Vergote, M., Vervier, M., Vianello, N., Viebke, H., Vilbrandt, R., Vorköper, A., Wadle, S., Wagner, F., Wang, E., Wang, N., Wang, Z., Warmer, F., Wauters, T., Wegener, L., Weggen, J., Wei, Y., Weir, G., Wendorf, J., Wenzel, U., Werner, A., White, A., Wiegel, B., Wilde, F., Windisch, T., Winkler, M., Winter, A., Winters, V., Wolf, S., Wolf, R.C., Wright, A., Wurden, G., Xanthopoulos, P., Yamada, H., Yamada, I., Yasuhara, R., Yokoyama, M., Zanini, M., Zarnstorff, M., Zeitler, A., Zhang, D., Zhang, H., Zhu, J., Zilker, M., Zocco, A., Zoletnik, S. & Zuin, M. 2019 Overview of first Wendelstein 7-X high-performance operation. *Nuclear Fusion* **59** (11), 112004.

Kornilov, V., Kleiber, R., Hatzky, R., Villard, L. & Jost, G. 2004 Gyrokinetic global three-dimensional simulations of linear ion-temperature-gradient modes in Wendelstein 7-X. *Physics of Plasmas* **11** (6), 3196–3202.

Kotschenreuther, M., Rewoldt, G. & Tang, W.M. 1995 Comparison of initial value and eigenvalue codes for kinetic toroidal plasma instabilities. *Computer Physics Communications* **88** (2-3), 128–140.

Lin, Z. 1998 Turbulent transport reduction by zonal flows: massively parallel simulations. *Science* **281** (5384), 1835–1837.

Maurer, M., Bañón-Navarro, A., Dannert, T., Restelli, M., Hindenlang, F., Görler, T., Told, D., Jarema, D., Merlo, G. & Jenko, F. 2020 GENE-3D: a global gyrokinetic turbulence code for stellarators. *Journal of Computational Physics* **420**, 109694.

Merz, F. 2009 Gyrokinetic simulation of multimode plasma turbulence. PhD thesis, Universität Münster.

Mishchenko, A., Helander, P. & Könies, A. 2008 Collisionless dynamics of zonal flows in stellarator geometry. *Physics of Plasmas* **15** (7), 072309.

Monreal, P., Calvo, I., Sánchez, E., Parra, F.I., Bustos, A., Könies, A., Kleiber, R. & Görler, T. 2016 Residual zonal flows in tokamaks and stellarators at arbitrary wavelengths. *Plasma Physics and Controlled Fusion* **58** (4), 045018.

Monreal, Pedro, Sánchez, Edilberto, Calvo, Iván, Bustos, Andrés, Parra, Félix I, Mishchenko, Alexey, Könies, Axel & Kleiber, Ralf 2017 Semianalytical calculation of the zonal-flow oscillation frequency in stellarators. *Plasma Physics and Controlled Fusion* **59** (6), 065005.

Parker, S.E., Lee, W.W. & Santoro, R.A. 1993 Gyrokinetic simulation of ion temperature gradient driven turbulence in 3D toroidal geometry. *Physical Review Letters* **71** (13), 2042–2045.

Peeters, A.G., Camenen, Y., Casson, F.J., Hornsby, W.A., Snodin, A.P., Strintzi, D.

& Szepesi, G. 2009 The nonlinear gyro-kinetic flux tube code GKW. *Computer Physics Communications* **180** (12), 2650–2672.

Proll, J.H.E. 2014 Trapped-particle instabilities in quasi-isodynamic stellarators. PhD thesis, Max-Planck-Institute für Plasmaphysik.

Proll, J.H.E, Mynick, H.E., Xanthopoulos, P., Lazerson, S.A. & Faber, B.J. 2015 TEM turbulence optimisation in stellarators. *Plasma Physics and Controlled Fusion* **58** (1), 014006.

Proll, J.H.E., Xanthopoulos, P. & Helander, P. 2013 Collisionless microinstabilities in stellarators. II. numerical simulations. *Physics of Plasmas* **20** (12), 122506.

Riemann, J., Kleiber, R. & Borchardt, M. 2016 Effects of radial electric fields on linear ITG instabilities in W7-X and LHD. *Plasma Physics and Controlled Fusion* **58** (7), 074001.

Rosenbluth, M.N. & Hinton, F.L. 1998 Poloidal flow driven by ion-temperature-gradient turbulence in tokamaks. *Physical Review Letters* **80** (4), 724–727.

Sánchez, E., García-Regaña, J.M., Navarro, A. Bañón, Proll, J.H.E., Moreno, C. Mora, González-Jerez, A., Calvo, I., Kleiber, R., Riemann, J., Smoniewski, J., Barnes, M. & Parra, F.I. 2021 Gyrokinetic simulations in stellarators using different computational domains. *Nuclear Fusion* **61** (11), 116074.

Smoniewski, J., Sánchez, E., Calvo, I., Pueschel, M. J. & Talmadge, J. N. 2021 Comparison of local and global gyrokinetic calculations of collisionless zonal flow damping in quasi-symmetric stellarators. *Physics of Plasmas* **28** (4), 042503.

Sugama, H. & Watanabe, T.-H. 2005 Dynamics of zonal flows in helical systems. *Physical Review Letters* **94** (11).

Sánchez, E., Mishchenko, A., García-Regaña, J.M., Kleiber, R., Bottino, A. & Villard, L. 2020 Nonlinear gyrokinetic PIC simulations in stellarators with the code EUTERPE. *Journal of Plasma Physics* **86** (5), 855860501.

Wang, H.Y., Holod, I., Lin, Z., Bao, J., Fu, J.Y., Liu, P.F., Nicolau, J.H., Spong, D. & Xiao, Y. 2020 Global gyrokinetic particle simulations of microturbulence in W7-X and LHD stellarators. *Physics of Plasmas* **27** (8), 082305.

Watanabe, T.H & Sugama, H. 2005 Velocity–space structures of distribution function in toroidal ion temperature gradient turbulence. *Nuclear Fusion* **46** (1), 24–32.

Wolf, R.C., Ali, A., Alonso, A., Baldzuhn, J., Beidler, C., Beurskens, M., Biedermann, C., Bosch, H.-S., Bozhenkov, S., Brakel, R., Dinklage, A., Feng, Y., Fuchert, G., Geiger, J., Grulke, O., Helander, P., Hirsch, M., Höfel, U., Jakubowski, M., Knauer, J., Kocsis, G., König, R., Kornejew, P., Krämer-Flecken, A., Krychowiak, M., Landreman, M., Langenberg, A., Laqua, H.P., Lazerson, S., Maassberg, H., Marsen, S., Marushchenko, M., Moseev, D., Niemann, H., Pablant, N., Pasch, E., Rahbarnia, K., Schlisio, G., Stange, T., Pedersen, T. Sunn, Svensson, J., Szepesi, T., Mora, H. Trimino, Turkin, Y., Wauters, T., Weir, G., Wenzel, U., Windisch, T., Wurden, G., Zhang, D., Abramovic, I., Äkäslompolo, S., Aleynikov, P., Aleynikova, K., Alzbutas, R., Anda, G., Andreeva, T., Ascasibar, E., Assmann, J., Baek, S.-G., Banduch, M., Barbui, T., Barlak, M., Baumann, K., Behr, W., Benndorf, A., Bertuch, O., Biel, W., Birus, D., Blackwell, B., Blanco, E., Blatzheim, M., Bluhm, T., Böckenhoff, D., Bolgert, P., Borchardt, M., Borsuk, V., Boscary, J., Böttger, L.-G., Brand, H., Brandt, Ch., Bräuer, T., Braune, H., Brezinsek, S., Brunner, K.-J., Brünner, B., Burhenn, R., Buttenschön, B., Bykov, V., Calvo, I., Cannas, B., Cappa, A., Carls, A., Carraro, L., Carvalho, B., Castejon, F., Charl, A., Chernyshev, F., Cianciosa, M., Citarella, R., Ciupiński, Ł., Claps, G., Cole, M., Cole, M.J., Cordella, F., Cseh, G., Czarnecka, A., Czermak, A., Czerski, K., Czerwinski, M., Czymek, G., da Molin, A., da Silva, A., Dammertz, G., de la Pena, A., Degenkolbe, S., Denner, P., Dhard, D.P., Dostal, M., Drevlak, M., Drewelow, P., Drews, Ph., Dudek, A., Dundulis, G., Durodie, F., van Eeten, P., Effenberg, F., Ehrke, G., Endler, M., Ennis, D., Erckmann, E., Esteban, H., Estrada, T., Fahrenkamp, N., Feist, J.-H., Fellinger, J., Fernandes, H., Fietz, W.H., Figacz, W., Fontdecaba, J., Ford, O., Fornal, T., Frerichs, H., Freund, A., Führer, M., Funaba, T., Galkowski, A., Gantenbein, G., Gao, Y., Regaña, J. García,

Garcia-Munoz, M., Gates, D., Gawlik, G., Geiger, B., Giannella, V., Gierse, N., Gogoleva, A., Goncalves, B., Goriaev, A., Gradic, D., Grahl, M., Green, J., Grosman, A., Grote, H., Gruca, M., Guerard, C., Haiduk, L., Han, X., Harberts, F., Harris, J.H., Hartfuss, H.-J., Hartmann, D., Hathiramani, D., Hein, B., Heinemann, B., Heitzenroeder, P., Henneberg, S., Hennig, C., Sanchez, J. Hernandez, Hidalgo, C., Hölbe, H., Hollfeld, K.P., Hölting, A., Höschen, D., Houry, M., Howard, J., Huang, X., Huber, M., Huber, V., Hunger, H., Ida, K., Ilkei, T., Illy, S., Israeli, B., Ivanov, A., Jablonski, S., Jagielski, J., Jelonnek, J., Jenzsch, H., Junghans, P., Kacmarczyk, J., Kaliatka, T., Kallmeyer, J.-P., Kamionka, U., Karalevicius, R., Kasahara, H., Kasparek, W., Kenmochi, N., Keunecke, M., Khilchenko, A., Kinna, D., Kleiber, R., Klinger, T., Knaup, M., Kobarg, Th., Köchl, F., Kolesnichenko, Y., Könies, A., Köppen, M., Koshurinov, J., Koslowski, R., Köster, F., Koziol, R., Krämer, M., Krampitz, R., Kraszewsk, P., Krawczyk, N., Kremeyer, T., Krings, Th., Krom, J., Krzesinski, G., Ksiazek, I., Kubkowska, M., Kühner, G., Kurki-Suonio, T., Kwak, S., Lang, R., Langish, S., Laqua, H., Laube, R., Lechte, C., Lennartz, M., Leonhardt, W., Lewerentz, L., Liang, Y., Linsmeier, Ch., Liu, S., Lobsien, J.-F., Loesser, D., Cisquella, J. Loizu, Lore, J., Lorenz, A., Losert, M., Lubyako, L., Lücke, A., Lumsdaine, A., Lutsenko, V., Majano-Brown, J., Marchuk, O., Mardenfeld, M., Marek, P., Massidda, S., Masuzaki, S., Maurer, D., McCarthy, K., McNeely, P., Meier, A., Mellein, D., Mendelevitch, B., Mertens, Ph., Mikkelsen, D., Mishchenko, O., Missal, B., Mittelstaedt, J., Mizuuchi, T., Mollen, A., Moncada, V., Mönnich, T., Morizaki, T., Munk, R., Murakami, S., Musielok, F., Náfrádi, G., Nagel, R., Naujoks, D., Neilson, H., Neubauer, O., Neuner, U., Ngo, T., Nocentini, R., Nührenberg, C., Nührenberg, J., Obermayer, S., Offermanns, G., Ogawa, K., Ongena, J., Oosterbeek, J.W., Orozco, G., Otte, M., Rodriguez, L. Pacios, Pan, W., Panadero, N., Alvarez, N. Panadero, Panin, A., Papenfuss, D., Paqay, S., Pavone, A., Pawelec, E., Pelka, G., Peng, X., Perseo, V., Peterson, B., Pieper, A., Pilopp, D., Pingel, S., Pisano, F., Plaum, B., Plunk, G., Povilaitis, M., Preinhaelter, J., Proll, J., Puiatti, M.-E., Sitjes, A. Puig, Purps, F., Rack, M., Récsei, S., Reiman, A., Reiter, D., Remppel, F., Renard, S., Riedl, R., Riemann, J., Rimkevicius, S., Risse, K., Rodatos, A., Röhlinger, H., Romé, M., Rong, P., Roscher, H.-J., Roth, B., Rudischhauser, L., Rummel, K., Rummel, T., Runov, A., Rust, N., Ryc, L., Ryosuke, S., Sakamoto, R., Samartsev, A., Sanchez, M., Sano, F., Satake, S., Satheeswaran, G., Schacht, J., Schauer, F., Scherer, T., Schlaich, A., Schlüter, K.-H., Schmitt, J., Schmitz, H., Schmitz, O., Schmuck, S., Schneider, M., Schneider, W., Scholz, M., Scholz, P., Schrittwieser, R., Schröder, M., Schröder, T., Schroeder, R., Schumacher, H., Schweer, B., Shanahan, B., Shikhovtsev, I.V., Sibilia, M., Sinha, P., Siplä, S., Skodzik, J., Slaby, C., Smith, H., Spiess, W., Spong, D.A., Spring, A., Stadler, R., Standley, B., Stephey, L., Stoneking, M., Stridde, U., Sulek, Z., Suzuki, Y., Szabó, V., Szabolics, T., Szökefalvi-Nagy, Z., Tamura, N., Terra, A., Terry, J., Thomas, J., Thomsen, H., Thumm, M., von Thun, C.P., Timmermann, D., Titus, P., Toi, K., Travere, J.M., Traverso, P., Tretter, J., Tsuchiya, H., Tsujimura, T., Tulipán, S., Turnyanskiy, M., Unterberg, B., Urban, J., Urbonavicius, E., Vakulchyk, I., Valet, S., van Millingen, B., Vela, L., Velasco, J.-L., Vergote, M., Vervier, M., Vianello, N., Viebke, H., Vilbrandt, R., Vorkörper, A., Wadle, S., Wagner, F., Wang, E., Wang, N., Warmer, F., Wegener, L., Weggen, J., Wei, Y., Wendorf, J., Werner, A., Wiegel, B., Wilde, F., Winkler, E., Winters, V., Wolf, S., Wolowski, J., Wright, A., Xanthopoulos, P., Yamada, H., Yamada, I., Yasuhara, R., Yokoyama, M., Zajac, J., Zarnstorff, M., Zeitler, A., Zhang, H., Zhu, J., Zilker, M., Zimbal, A., Zocco, A., Zoletnik, S. & Zuin, M. 2017 Major results from the first plasma campaign of the Wendelstein 7-X stellarator. *Nuclear Fusion* **57** (10), 102020.

Xanthopoulos, P. & Jenko, F. 2007 Gyrokinetic analysis of linear microinstabilities for the stellarator Wendelstein 7-X. *Physics of Plasmas* **14** (4), 042501.

Xanthopoulos, P., Merz, F., Görler, T. & Jenko, F. 2007 Nonlinear gyrokinetic

simulations of ion-temperature-gradient turbulence for the optimized Wendelstein 7-X stellarator. *Physical Review Letters* **99** (3).

XANTHOPOULOS, P., MISCHCHENKO, A., HELANDER, P., SUGAMA, H. & WATANABE, T.-H. 2011 Zonal flow dynamics and control of turbulent transport in stellarators. *Physical Review Letters* **107** (24).